

## INFRARED SPECTRA AND PHOTOMETRY OF COMPLETE SAMPLES OF PG AND 2MASS QUASARS

SHI, YONG<sup>1,2</sup>, RIEKE, G. H.<sup>3</sup>, OGLE, P. M.<sup>4</sup>, SU, K. Y. L.<sup>3</sup>, & BALOG, Z.<sup>5</sup>*Draft version August 27, 2014*

## ABSTRACT

As a step toward a comprehensive overview of the infrared diagnostics of the central engines and host galaxies of quasars at low redshift, we present *Spitzer* Space Telescope spectroscopic (5–40  $\mu\text{m}$ ) and photometric (24, 70 and 160  $\mu\text{m}$ ) measurements of all Palomar-Green (PG) quasars at  $z < 0.5$  and 2MASS quasars at  $z < 0.3$ . We supplement these data with *IRAS* and *ISO* data and with *Herschel* measurements at 160  $\mu\text{m}$ . The sample is composed of 87 optically selected PG quasars and 52 near-IR selected 2MASS quasars. Here we present the data, measure the prominent spectral features, and separate emission due to star formation from that emitted by the dusty circumnuclear torus. We find that the mid-IR (5–30  $\mu\text{m}$ ) spectral shape for the torus is largely independent of quasar IR luminosity with scatter in the SED shape of  $\lesssim 0.2$  dex. Except for the silicate features, no large difference is observed between PG (unobscured - silicate emission) and 2MASS (obscured - silicate absorption) quasars. Only mild silicate features are observed in both cases. When in emission, the peak wavelength of the silicate feature tends to be longer than 9.7  $\mu\text{m}$ , possibly indicating effects on grain properties near the AGN. The IR color is shown to correlate with the equivalent width of the aromatic features, indicating that the slope of the quasar mid- to far-IR SED is to first order driven by the fraction of radiation from star formation in the IR bands.

*Subject headings:* infrared: galaxies – galaxies: active – galaxies: starburst

## 1. INTRODUCTION

Active galactic nuclei, signposts for accretion onto super-massive black holes (SMBHs), are now understood to be a critical phase of massive galaxy formation. In the local universe all individual massive galaxies are found to host SMBHs at their centers, with the SMBH masses tightly correlated with galaxy properties (Kormendy & Richstone 1995; Magorrian et al. 1998; Gebhardt et al. 2000; Ferrarese & Merritt 2000). Probing the properties of material located at different radii surrounding SMBHs should offer important clues to how accretion by the SMBHs influences, or is influenced by, the evolution of their host galaxies to maintain this correlation. It may also solve puzzles such as how the angular momentum of material at kpc radii is removed to feed central engines.

It is believed that there is a geometrically thick structure, termed the dusty torus, outside the accretion disk in AGNs. The dusty torus may physically bridge from the inner accretion disk to the outer host galaxy, and likely plays a crucial role in funnelling the material into SMBHs. Significant progress has been made in probing the torus, starting from the earliest suggestions of its existence in the 1980's to direct imaging of it in a few nearby AGN (Jaffe et al. 2004). The dusty torus is thought to explain the large apparent diversity of AGN

phenomena. For example, in the AGN unified model (Antonucci 1993), orientation-dependent obscuration in the torus determines whether the broad emission lines emerge in the UV/optical spectra and thus whether an AGN is classified as type 1 or type 2.

The dust in the torus is heated by UV/optical radiation from the accretion disk to high temperatures ( $\sim 100$ – $1000$  K) to emit dominantly in the near- to mid-IR spectral ranges. The emission by the torus dust is dominated by a continuum that is featureless, except for the broad silicate features at around 9.7 and 18  $\mu\text{m}$  either in emission or absorption. Its output is distinct from the radiation of star-forming regions: for them, the aromatic features dominate at wavelengths shorter than 15  $\mu\text{m}$ , while at longer wavelengths there is a strong continuum due to warm and cold ( $< 60$  K) dust (Smith et al. 2007; Stierwalt et al. 2013). In luminous AGN, i.e. quasars such as those studied here, does the torus nearly always dominate the integrated mid-IR emission so that the observations can be compared directly to predictions of torus models.

The silicate features are important diagnostics to constrain the structure of the dusty torus (Siebenmorgen et al. 2005; Hao et al. 2005; Sturm et al. 2005, 2006; Shi et al. 2006). They can be directly compared to predictions of dusty torus models, probing the internal torus structures (Fritz et al. 2006; Hönig et al. 2006; Nenkova et al. 2008; Schartmann et al. 2008; Stalevski et al. 2012; Feltre et al. 2012). For example, Feltre et al. (2012) demonstrate how to discriminate two broad types of dusty tori, i.e., smooth vs. clumpy, through the behavior of the silicate features and of the overall mid-IR SEDs. The IR emission lines also have the advantage of probing narrow emission line regions without significant extinction (e.g. Diamond-Stanic et al. 2009).

The infrared data are also powerful in probing the

<sup>1</sup> School of Astronomy and Space Science, Nanjing University, Nanjing 210093, China

<sup>2</sup> Key Laboratory of Modern Astronomy and Astrophysics (Nanjing University), Ministry of Education, Nanjing 210093, China

<sup>3</sup> Department Of Astronomy And Steward Observatory, University of Arizona, 933 N Cherry Ave, Tucson, AZ 85721, USA

<sup>4</sup> Infrared Processing and Analysis Center, California Institute of Technology, 1200 East California Boulevard, Pasadena, CA 91125, USA

<sup>5</sup> Max-Planck-Institut für Astronomie, Königstuhl 17, D-69117 Heidelberg Germany

host galaxy properties, e.g. the star formation rate (SFR). While commonly used SFR tracers, such as UV radiation, hydrogen recombination lines, and forbidden lines are contaminated severely by the nuclear radiation, the mid-IR aromatic features and far-IR photometry are two relatively uncontaminated tracers of star formation in quasars (e.g. Shi et al. 2007; Netzer et al. 2007; Lutz et al. 2008; Hernán-Caballero et al. 2009; Hiner et al. 2009; Rosario et al. 2013).

Studies of infrared features are enabled by the *Spitzer* Space Telescope with a photometric wavelength coverage from 3.6 to 160  $\mu\text{m}$  and low resolution spectroscopy from 5 to 40  $\mu\text{m}$ . To exploit the potential of the infrared data, we carried out a program with *Spitzer* in the last cryogenic cycle to complete spectroscopic (5-40  $\mu\text{m}$ ) and photometric (24, 70 and 160  $\mu\text{m}$ ) observations of two samples of luminous AGNs at low redshift, namely the unobscured optically selected Palomar-Green (PG) quasars (Schmidt & Green 1983; Boroson & Green 1992) and obscured near-IR selected 2MASS quasars (Cutri et al. 2001; Smith et al. 2002). By focusing on quasars, we will probe the phase where SMBHs grow most rapidly and where their output stands out most clearly from that of their host galaxies.

In this paper we present the observations and extract measurements of aromatic and silicate features and continuum luminosities for these two samples. We use this information to determine the SFRs of the host galaxies and to show that the values from the aromatic bands and far infrared emission are consistent. We present the sample, observations, and data reductions in § 2. The spectral decomposition is detailed in § 3. The results are presented in § 4. Our conclusions are presented in § 5. Throughout this paper, we assume  $H_0=70 \text{ km s}^{-1} \text{ Mpc}^{-1}$ ,  $\Omega_0=0.3$  and  $\Omega_\Lambda=0.7$ .

## 2. SAMPLES, OBSERVATIONS AND DATA REDUCTION

### 2.1. Samples

For this study we included all 87 objects of the PG sample (Schmidt & Green 1983; Boroson & Green 1992) at  $z < 0.5$  and all 52 objects of the 2MASS sample (Cutri et al. 2001; Smith et al. 2002) at  $z < 0.3$ , as listed in Table 1. The PG quasars are defined by an average limiting  $B$  band magnitude of 16.16, blue  $U-B$  color ( $< -0.44$ ), and dominant star-like appearance. All these objects show broad emission lines, and thus are classified as type 1 quasars. Due to the large photographic magnitude errors and the simple color selection, the PG sample is incomplete (e.g. Goldschmidt et al. 1992; Jester et al. 2005), but the incompleteness is independent of the optical magnitude and color (Jester et al. 2005), indicating that the PG sample is still representative of bright optically selected quasars. Compared to PG quasars, the 2MASS quasars represent a redder population with  $J-K_s > 2$  (compared with a typical value of  $J-K_s \sim 1.5$  for PG quasars), but have similar  $K_s$ -band luminosities ( $M_{K_s} < -23$ ) (Smith et al. 2002). Unlike PG quasars the 2MASS sample includes objects with narrow, intermediate and broad emission lines. The 2MASS sample is increasingly incomplete at  $K_s > 13$  (Cutri et al. 2001).

### 2.2. Observations And Data Reduction

We carried out 25.1 hr of *Spitzer* observations (PID: 50196; PI: G. Rieke) to complete the IRS spectroscopic

and MIPS photometric data for the PG/2MASS sample. The program included all objects that did not have archived data from previous cycles. As a result, there are low resolution infrared spectra (5-40  $\mu\text{m}$ ) and MIPS photometry at 24, 70 and 160  $\mu\text{m}$  for the entire sample.<sup>6</sup> All the broad-band photometry is listed in Table 2, while the IRS data are available in Table 3.

The spectra were obtained using the standard IRS staring mode. To reduce them, we drew from the archive the basic calibrated data (BCD) as products of *Spitzer* Science Center data reduction pipeline version S18.7, which provided cosmic ray removal, replacement of saturated pixels, droop correction, subtraction of darks, linearization correction, and stray light and flat field correction. The post-pipeline processing of the BCD was based on IRSCLEAN<sup>7</sup> and SPICE<sup>8</sup>. IRSCLEAN was used to create bad pixel masks for the BCD image. The sky background for each module within a given order was then subtracted using the image obtained with the same module in a different order. For observations with only one order, the image at one slit position was used as sky background for the image at another slit position. SPICE was employed to extract the spectra from these background-subtracted images. We used the optimal extraction mode to increase the ratio of signal to noise, since our targets are point sources. The mismatch in the signal between short-low (5-14  $\mu\text{m}$ ) and long-low (14-40  $\mu\text{m}$ ) modules was removed by scaling the short-low spectrum to the long-low one. The whole spectrum was further scaled to the MIPS 24  $\mu\text{m}$  photometry by comparing to synthetic photometry of the spectra. The flux difference between the short-low and long-low, and the difference between the MIPS 24  $\mu\text{m}$  photometry and IRS synthetic flux at this wavelength, could be caused by the errors in the flux calibration of the MIPS and IRS instruments, and the pointing errors with short-low and long-low, not necessarily by extended emission outside the IRS slit. As listed in Table 2, the scaling factor from short-low to long-low has a median value of 1.0 and a standard deviation of 0.4, and the factor from long-low synthetic 24  $\mu\text{m}$  to MIPS 24  $\mu\text{m}$  flux has a median value of 1.08 and a standard deviation of 0.18. The almost unity conversion factor with scatter comparable to the flux calibration uncertainties indicates that missed extended emission is not important for the IRS observations. In addition, visual checks of MIPS 24  $\mu\text{m}$  images do not find any source with significant extended emission.

MIPS observations were made with the small field photometry mode. The data reduction and photometry measurements were carried out with Data Analysis Tool v3.1 and redMIPS v1.1 (Gordon et al. 2005) by the MIPS Instrument Team. For the 160  $\mu\text{m}$  photometry, we have visually checked individual images and removed those

<sup>6</sup> The previous IRS spectroscopic programs were by J. Houck (PID: 4), G. Rieke (PID: 36), F. Low (PID: 40), M. Werner (PID: 61), S. Gallagher (PID: 148), R. Siebenmorgen (PID: 193), D. Lutz (PID: 323), S. Veilleux (PID: 485), A. Stockton (PID: 14067), A. Wehrle (PID: 14991) and particularly by P. Ogle (PID: 11451). The previous MIPS programs were led by F. Low (PID: 49), G. Rieke (PID: 82, 30306, 40053, 50507), M. Werner (PID: 86), M. Bondi (PID: 3327), M. Bondi (PID: 3327), Z. Shang (PID: 20084), A. Marscher (PID: 20496), A. Wehrle (PID: 30785), G. Fazio (PID: 30860).

<sup>7</sup> <http://irsa.ipac.caltech.edu/data/SPITZER/docs/dataanalysis tools/tools/irsa/>

<sup>8</sup> <http://irsa.ipac.caltech.edu/data/SPITZER/docs/dataanalysis tools/tools/irsa/>

where the photometry is affected by close companions or structure in the sky (e.g., IR cirrus). In total 98%, 91% and 32% of the sample have MIPS detections above  $3\sigma$  at 24, 70 and 160  $\mu\text{m}$ , respectively.

To increase the fraction of objects with 160  $\mu\text{m}$  detections, we searched for measurements in the *Herschel* Space Telescope data archive. All the PG quasars have been observed with *Herschel* (PI: L. Ho) but no archived data were found for the 2MASS quasars. These data were reduced to images as described in Balog et al. (2013). First, bad and saturated pixels were flagged. The response was calibrated and corrected for flat fields. A high-pass filter was applied to eliminate the  $1/f$  noise of the detector. Aperture photometry was carried out on the reduced images as in Balog et al. (2013). For objects with both *Spitzer* 160  $\mu\text{m}$  and *Herschel* 160  $\mu\text{m}$  detections, the latter is used because of (generally) higher signal-to-noise and greater freedom from structured sky emission.

### 3. SPECTRAL DECOMPOSITIONS

#### 3.1. Fitting spectral features

The infrared spectra of quasars are rich in features. As shown in Fig. 1, they usually contain strong hot dust continuum emission, cold dust emission, silicate emission or absorption features at 9.7 and 18  $\mu\text{m}$ , aromatic features mainly at 6.2, 7.7, 8.6, 11.3 and 12.1  $\mu\text{m}$ , plus atomic fine-structure and molecular hydrogen emission lines.

Although these features can be measured individually, we prefer to fit them simultaneously so that blends can be separated. Our method is based on a simple physical model, similar to the IDL program PAHFIT.pro that was developed by Smith et al. (2007) to decompose the spectra of normal galaxies. The dust continuum is modelled through a combination of a series of black-bodies at fixed temperatures of 1000, 580, 415, 210, 97, 58, 48, 41, 32, 29 and 26 K while letting the normalization be free. The highest temperature is chosen to fit the hottest dust emission peaking around 3  $\mu\text{m}$ , and the lowest temperature is limited by our SED coverage that in general does not extend beyond 200  $\mu\text{m}$ . This set of temperatures was based on several test runs, and includes criteria such as the peak wavelengths of the black-bodies should not lie within spectral regions of strong and broad silicate and aromatic features. The emission at wavelengths longer than 200  $\mu\text{m}$  is usually described by a modified black-body. However, as we have little  $> 200$   $\mu\text{m}$  photometry and are not fitting features in this spectral range, we simply adopted black-body spectra. Higher-fidelity fits to these long wavelengths are discussed in the following section. Each silicate feature either in emission or absorption is modelled through two Gaussian functions: 1.) for the 9.7  $\mu\text{m}$  silicate feature, central wavelengths of two Gaussians were set to be 10.0 and 11.5  $\mu\text{m}$  that can vary by  $\pm 3\%$ . The standard deviations (i.e., widths) were set to be 8% and 10% of the central wavelengths, respectively. The fractional Gaussian widths were allowed to vary from -2% to +4%. The normalizations of the two Gaussians are free, with the initial value set to be half of the difference between the observed flux at the Gaussian central wavelength and the one at 8  $\mu\text{m}$ ; and 2.) for the 18  $\mu\text{m}$  feature, two Gaussians were placed at 16.0 and 19.0  $\mu\text{m}$ , respectively, with all other parameters treated similarly to those for the 9.7  $\mu\text{m}$  feature;

the initial value of the normalization is set to be half of the difference between the observed flux at the Gaussian central wavelength and the one at 15  $\mu\text{m}$ . Figure 2 shows examples of the two-Gaussian fitting for the 9.7 silicate feature. A single Gaussian function was used to model the emission lines including  $\text{H}_2$  S(3) 9.67  $\mu\text{m}$ , [SIV] 10.52  $\mu\text{m}$ , [NeII] 12.81  $\mu\text{m}$ , [NeIII] 15.56  $\mu\text{m}$ ,  $\text{H}_2$  S(1) 17.03  $\mu\text{m}$  and [OIV] 25.91  $\mu\text{m}$ . The line width of the Gaussian was set by the spectral resolution at a given wavelength but allowed to vary by  $\pm 20\%$ , while the normalization was totally free. As detailed in Smith et al. (2007), the aromatic features were described by Drude profiles with fixed centers and widths but free normalizations.

The fitting results from minimizing  $\chi^2$  were in general excellent under visual inspection. However, for about 20% of the sample, the broad silicate emission features appeared to mimic dust black-body emission. In these cases, the initial value of the silicate feature strength needs to be relatively accurate and was obtained by spline interpolation or visual estimate. We used a general criterion that the dust continuum underlying the silicate emission feature between 9 and 20  $\mu\text{m}$  should change gradually and monotonically.

The results of the SED decompositions are shown in Fig. 1. With the fitted profiles, various features are quantified and listed in Table 4. The silicate feature strength is defined as  $\ln(f^{\text{peak}}/f_{\text{cont}}^{\text{peak}})$  where  $f^{\text{peak}}$  is the flux density at the wavelength where the silicate emission feature peaks or the silicate absorption feature shows a minimum based on the two fitted Gaussian profiles for the individual features, and  $f_{\text{cont}}^{\text{peak}}$  is the continuum flux density at the same wavelength. The continuum luminosities at given wavelengths were measured as the average of the spectra over a 2  $\mu\text{m}$  range around the central wavelengths. All the listed errors in Table 4 only consider the photon noise in the spectrum. For the silicate feature intensity, due to the difficulty in differentiating the broad feature from the underlying continuum, there are additional systematic uncertainties that could be up to 0.1-0.2. The peak wavelength can also suffer systematic errors of  $\sim 1$   $\mu\text{m}$  for the 9.7  $\mu\text{m}$  feature and 2  $\mu\text{m}$  for the 18  $\mu\text{m}$  silicate feature.

#### 3.2. Decomposing SEDs into star-forming and dusty torus components

The above spectral decomposition aims to measure intensities of different spectral features. In this section we decompose the full IR SED into emission from star formation and the radiation from the dusty torus. For an initial reconnaissance, we assume the emission at a far-IR wavelength or an aromatic feature comes entirely from star-forming regions and then select the star-forming template (Rieke et al. 2009) that yields the closest observed fluxes. We have derived such estimates in three ways: 1.) 11.3  $\mu\text{m}$  aromatic features; 2.) MIPS 70  $\mu\text{m}$  photometry; and 3.) MIPS or PACS 160  $\mu\text{m}$  photometry.

Although the aromatic features in quasar spectra arise from star formation regions in the host galaxies (e.g. Shi et al. 2007), observations of the central regions ( $\sim 0.5$  kpc) of Seyfert galaxies indicate that the nuclear radiation may suppress the aromatic features at 6.2, 7.7 and 8.6  $\mu\text{m}$ , but not the 11.3  $\mu\text{m}$  feature (Diamond-Stanic & Rieke 2010; Esquej et al. 2014). We

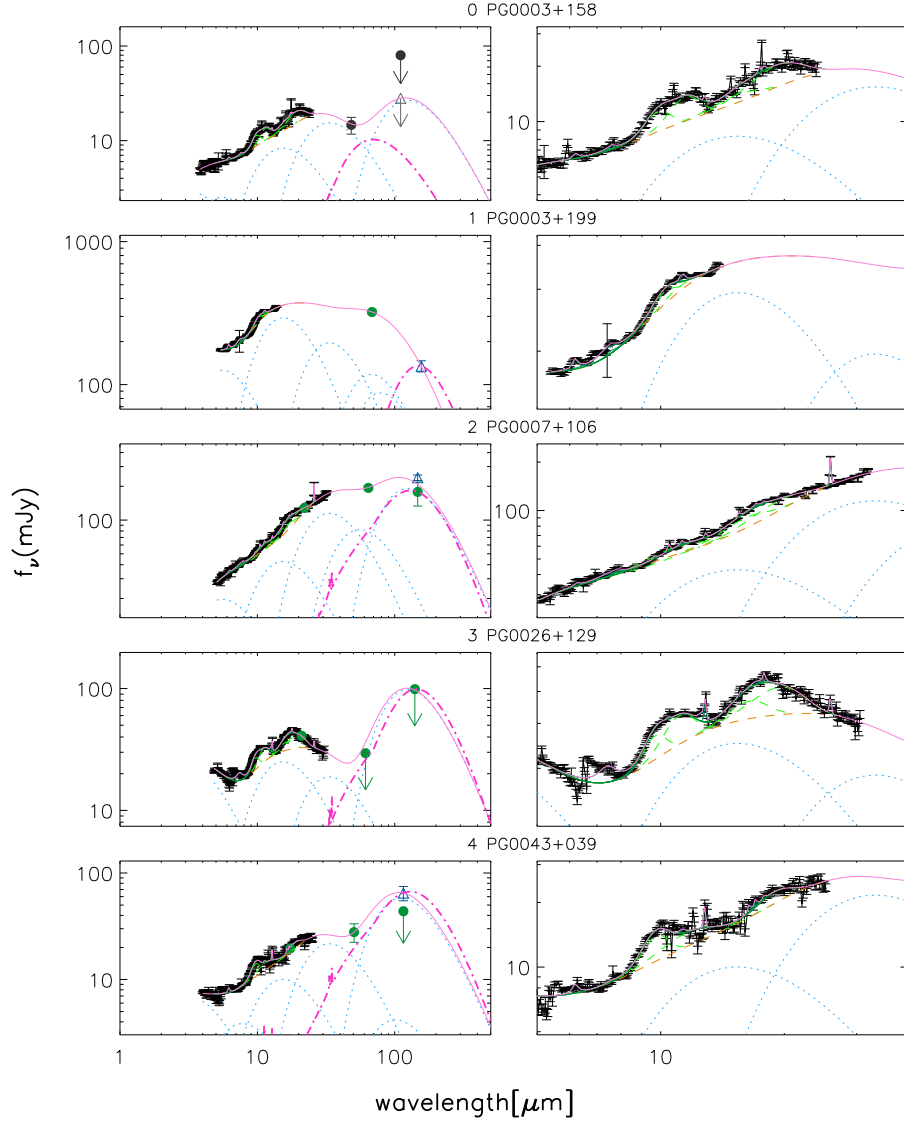


FIG. 1.— The rest-frame IRS spectra (black points) and broad-band photometry (green filled circles). For each object, the left panel shows the full SEDs while the right panel zooms into the 5 to 40  $\mu\text{m}$  spectral range. The pink solid lines are the fitted curves as a sum of all individual fitted profiles including black-body, silicate features, aromatic features and emission lines. The blue dotted lines indicate the fitted individual black-body emission the sum of which is shown as yellow dashed line. The green dashed lines represent the fitted silicate feature profiles. The pink dotted-dashed line is the best-fit star-forming template derived from the library of Rieke et al. (2009).

convert the aromatic flux for this feature to SFR using the star-forming templates of Rieke et al. (2009). An issue with this method is the large intrinsic scatter between aromatic fluxes and star formation rates as seen in non-AGN star-forming galaxies (Smith et al. 2007; Calzetti et al. 2007).

Far infrared luminosity is generally considered to be a reliable SFR indicator for galaxies. For each broad-band photometry measurement, we choose the star-forming template with monochromatic luminosity closest to the observation, normalize it to the measured flux density, and estimate the FIR luminosity from this normalized template. The risk for this approach is that the far-IR emission may be contaminated by cold dust in the dusty torus. After choosing the best star-forming template, including bands not affected by cold ISM dust, we measured the SFRs based on the 24  $\mu\text{m}$  emission of the template following Rieke et al. (2009).

We evaluate the contribution from the dusty torus to the 70 and 160  $\mu\text{m}$  emission by comparing SFRs from these two bands to the aromatic-based SFRs, since the aromatic emission should arise mainly from star forming regions. Although aromatic features could be excited by B-type stars (Peeters et al. 2004; Vega et al. 2010), for our sample with relatively high far-IR luminosity (mostly above  $10^{10} L_{\odot}$ ), such a contribution should be negligible. As shown in Figure 3, no systematic offset is seen between 160 $\mu\text{m}$ -based SFRs and the SFRs from aromatic features. The situation for the 70 $\mu\text{m}$ -based SFRs is more complex. For SFRs larger than  $10 M_{\odot}/\text{yr}$  from the aromatic feature, there is no systematic offset. For lower SFRs, the estimates from the 70 $\mu\text{m}$  measurement tend to be high. This behavior may indicate contamination of the 70  $\mu\text{m}$  photometry (typically at rest frame  $\sim 50 \mu\text{m}$  for our sample) by emission from the dusty torus in cases where the SFR is low.



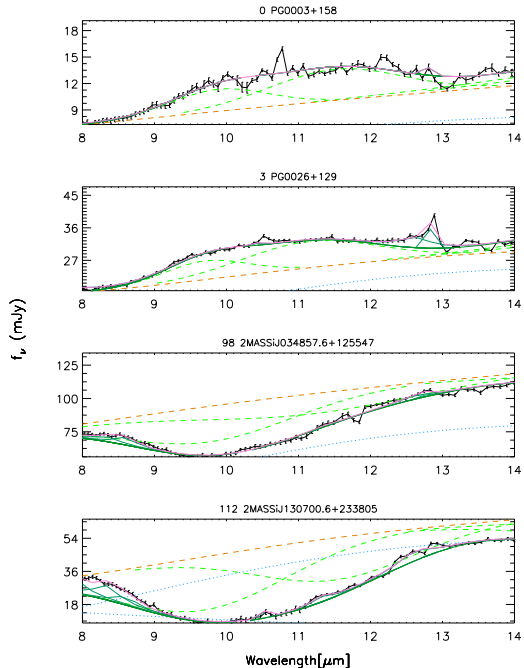


FIG. 2.— Examples of two Gaussian fitting for the  $9.7 \mu\text{m}$  silicate feature. All line styles are the same as the Figure 1.

The above three methods demonstrate the overall consistency of SFRs estimated from monochromatic photometry or a single aromatic feature. Therefore, it is permissible to improve the accuracy in the SFR estimates by combining the three methods through template fitting. For objects with  $160 \mu\text{m}$  detections, a first-guess star-forming template is chosen to have the closest  $160 \mu\text{m}$  luminosity to the observation. If this template, however, produces higher  $70 \mu\text{m}$  luminosity than is observed, we discard it and instead choose the next colder template in the library of Rieke et al. (2009). Sometimes this process needs to be repeated until the best template is chosen. Similarly, for objects with  $70 \mu\text{m}$  detections, the best star-forming template is the one that has the closest  $70 \mu\text{m}$  luminosity to the observation. But, if the template produces  $160 \mu\text{m}$  output above the observed upper-limit, a hotter template is chosen. As indicated in Figure 3, for  $70 \mu\text{m}$  based SFRs smaller than  $10 M_{\odot}/\text{yr}$ , we reduce the SFR estimate by 0.3 dex to account statistically for the torus emission. For objects with aromatic features, the best-fit template is required to not exceed the 70 and  $160 \mu\text{m}$  upper-limits; if it does it is renormalized to lower its luminosity and make it consistent. The estimated SFRs are listed in Table 4. Both quasar samples have SFR measurements for as many as 94% of the members, with upper limits for the rest. We assigned a systematic error of 0.3 dex for  $160 \mu\text{m}$  based SFRs as well as  $70 \mu\text{m}$  based SFRs above  $10 M_{\odot}/\text{yr}$ , and 0.5 dex for  $70 \mu\text{m}$  based SFRs below  $10 M_{\odot}/\text{yr}$  as well as aromatic based SFRs, based on the scatter of Figure 3. Fig. 1 shows the best-fit star-forming template for each quasar. The residual after subtracting the star-forming template is adopted as the radiation from the dusty torus.

#### 4. RESULTS

##### 4.1. Composite Quasar SEDs and Scatter About Them

Figure 5 shows the median composite spectra with  $1\text{-}\sigma$  scatter for the PG and 2MASS samples normalized at  $14\text{--}16 \mu\text{m}$ . The composite spectrum from  $5$  to  $25 \mu\text{m}$  is derived by taking the median of the spectroscopic data projected to a common wavelength grid with a spectral resolution of 50. We took the median of all the  $70 \mu\text{m}$  photometry with the rest-frame wavelength from  $40$  to  $70 \mu\text{m}$  as the composite flux density at  $55 \mu\text{m}$ , and that of  $160 \mu\text{m}$  data with the rest-frame wavelength from  $100$  to  $160 \mu\text{m}$  as the composite flux density at  $130 \mu\text{m}$ . We also constructed composite spectra for the radio quiet and radio loud sub-samples of PG objects, where the radio loudness data are from Kellermann et al. (1989), as indicated in Table 5. All the PG objects have mid-IR spectroscopic measurements while 90% and 76% of the sample have detections at  $70$  and  $160 \mu\text{m}$ , respectively. 95% of the 2MASS sample have mid-IR spectroscopic measurements and  $70 \mu\text{m}$  detections, with  $160 \mu\text{m}$  detections for 33%. The median spectra presented in Fig. 5 should be representative of the whole PG sample up to rest-frame  $130 \mu\text{m}$  and of the 2MASS sample to rest-frame  $60 \mu\text{m}$ , while the rest-frame  $130 \mu\text{m}$  data point of the 2MASS median spectrum should be biased by the far-IR luminous objects in the sample. There are some differences in the median spectra between the 2MASS and PG samples. While the PG median spectrum shows silicate emission, the 2MASS one has silicate absorption, consistent with the near-IR selected 2MASS quasars being viewed on average more edge-on. In addition, the 2MASS spectrum has much larger EWs of the aromatic features compared to the PG spectrum, as well as elevated rest-frame  $60 \mu\text{m}$  emission relative to the mid-IR. This behavior indicates more active star formation relative to the nuclear SMBH luminosity in 2MASS quasar host galaxies (Shi et al. 2007).

Figure 3 compares the SEDs we have determined with a number of alternatives. Elvis et al. (1994) presented composite SEDs of 47 non-blazar quasars, largely based on members of the PG sample. Their IR data are based on ground-based N and Q bands ( $10$  and  $20 \mu\text{m}$ ) as well as IRAS broad-band photometry ( $12$ ,  $25$ ,  $60$  &  $100 \mu\text{m}$ ). As shown in Figure 5, their radio-quiet composite SED shows an overall similar shape to that of radio-quiet PG quasars from our work below rest-frame  $60 \mu\text{m}$  but is significantly lower at rest-frame  $130 \mu\text{m}$ . However, their data do not include photometry at wavelengths longer than observed-frame  $100 \mu\text{m}$  and the SED at longer wavelengths is based on extrapolation. On the other hand, their radio-loud quasar composite SED is similar to ours between rest-frame  $5$  and  $130 \mu\text{m}$ . Richards et al. (2006) compiled *Spitzer* broad-band photometry of 259 SDSS-selected optically bright quasars at  $3.6$ ,  $4.5$ ,  $5.8$ ,  $8.0$ ,  $24$  and  $70 \mu\text{m}$ . Their sample covers a redshift range from  $z=0$  up to  $z=4$ . Compared to our composite spectrum of all PG quasars, their SED shows an overall similar shape between rest-frame  $5$  and  $30 \mu\text{m}$  but lacks silicate emission features. Above rest-frame  $100 \mu\text{m}$ , their SED drops faster than ours. Again, their observations do not contain far-IR data above observed  $70 \mu\text{m}$  and the shape at longer wavelengths is based on extrapolation. Netzer et al. (2007) constructed the intrinsic quasar SED of 8 PG quasars after removing the star-forming emission. Their SED resembles our composite spectrum for the whole PG sample up to  $30 \mu\text{m}$  above which theirs

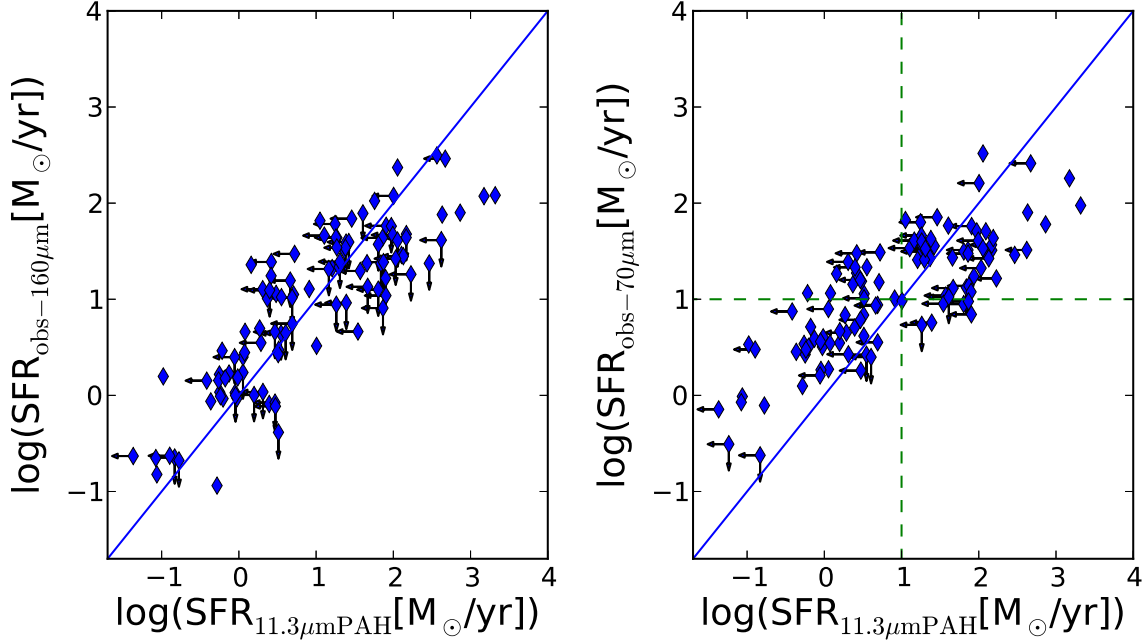


FIG. 3.— Comparisons between different SFR estimates: the left panel shows the comparison between estimates from the  $160\ \mu\text{m}$  and aromatic feature measurements; the right panel shows the comparison between  $70\ \mu\text{m}$ -based and aromatic-feature-based SFR estimates.

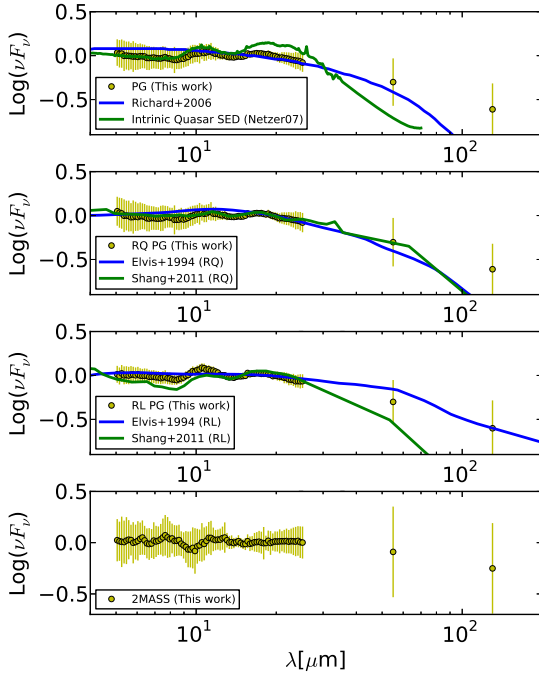


FIG. 4.— From top to bottom, filled circles indicate composite median SEDs of all PG quasars, radio quiet PG quasars, radio loud PG quasars and all 2MASS quasars, respectively, where the error bar is shown at  $1\text{-}\sigma$  level. The comparison SEDs include those by Elvis et al. (1994), Richards et al. (2006), Netzer et al. (2007) and Shang et al. (2011).

drops much faster, which is expected as the star-forming radiation starts to dominate the infrared emission above  $30\ \mu\text{m}$ . Shang et al. (2011) constructed a composite SED of 85 optically bright, non-blazar quasars that are selected heterogeneously. Their radio-quiet composite SED is quite similar to our radio-quiet PG spectrum between rest-frame 5 and  $30\ \mu\text{m}$  but drops faster longward of rest-frame  $55\ \mu\text{m}$ , which is also the case when compar-

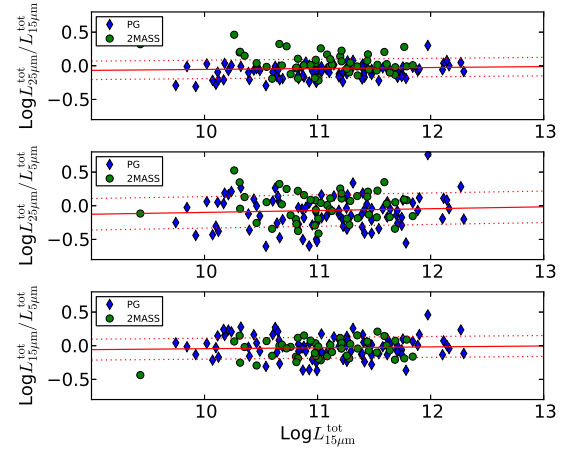


FIG. 5.— The mid-IR color of  $25\mu\text{m}/15\mu\text{m}$ ,  $25\mu\text{m}/5\mu\text{m}$ ,  $15\mu\text{m}/5\mu\text{m}$  as a function of the  $15\ \mu\text{m}$  luminosity. All luminosities are monochromatic emission averaged over  $2\ \mu\text{m}$  width of the central wavelength. The best linear fits are shown as solid lines with  $1\text{-}\sigma$  scatter as the dotted line. The fitting results are also listed in Table 6.

ing their radio-loud composite SED to our radio-loud PG one. The comparison of  $160\ \mu\text{m}$  photometry for about 20 objects in common reveals that their measurements are systematically lower than ours by a factor of a few. Since our independent measurements at this wavelength from *Spitzer* and *Herschel* agree much more closely than this factor, we believe our measurements are reliable.

To illustrate the scatter of the mid-IR spectra among the whole PG and 2MASS samples, we present the relationships between infrared color as a function of  $15\ \mu\text{m}$  monochromatic luminosities in Figure 5 and list the best-fit linear relations in Table 6. Almost zero slopes for all of these relationships indicate that the mid-IR spectral shape of PG and 2MASS quasars are roughly independent of quasar mid-IR luminosities. In addition, the scatter of the relationship is quite small, ranging from 0.14 to

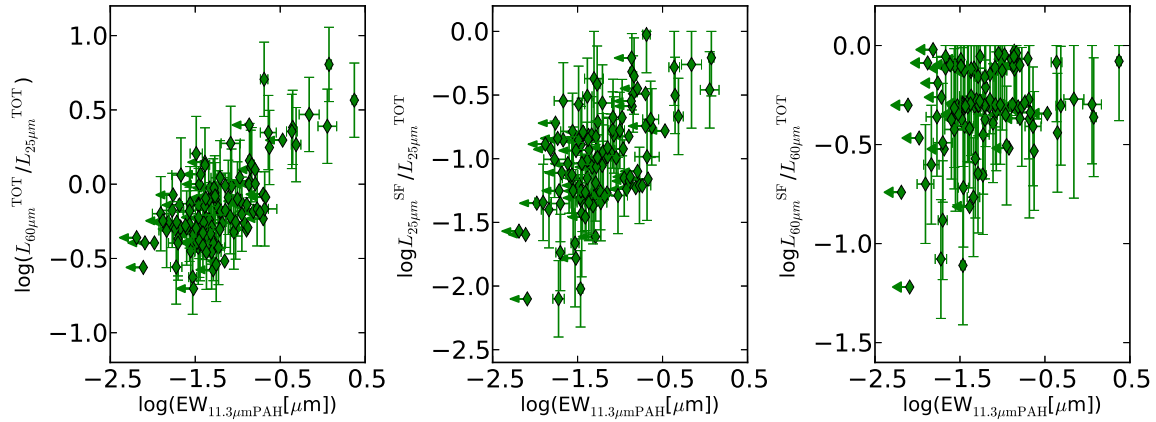


FIG. 6.— *Left Panel:* The IR color ( $L_{60\mu\text{m}}^{\text{TOT}}/L_{25\mu\text{m}}^{\text{TOT}}$ ) as a function of the  $11.3\mu\text{m}$  aromatic feature equivalent width. *Middle Panel:* The fraction of  $25\mu\text{m}$  emission from star formation as a function of the  $11.3\mu\text{m}$  aromatic feature equivalent width. *Right Panel:* The fraction of  $60\mu\text{m}$  emission from star formation as a function of the  $11.3\mu\text{m}$  aromatic feature equivalent width.

0.23 dex. This suggests that the composite mid-IR spectra derived above are good representatives of quasar mid-IR spectra independent of quasar IR luminosities and quasar types. However, these spectra include combinations of SMBH- and SF-generated components, as would also be the case for the previously determined quasar spectral templates (e.g. Elvis et al. 1994; Richards et al. 2006; Shang et al. 2011). Obtaining an intrinsic quasar SED template in the far infrared requires subtracting the SF contribution.

#### 4.2. Contribution of Star Formation to the SED

The left panel of Figure 6 shows the IR color  $\log(L_{60\mu\text{m}}/L_{25\mu\text{m}})$  as a function of the EW of the  $11.3\mu\text{m}$  aromatic feature. This color varies from -0.8 to 0.8 for the whole quasar sample, but it clusters in a smaller range from -0.5 to 0.25. The  $\text{EW}_{11.3\mu\text{mPAH}}$  for the sample ranges from  $<0.003\mu\text{m}$  to  $2.3\mu\text{m}$ . As shown in the figure, the two quantities are roughly related to each other, with increasing  $\log(L_{60\mu\text{m}}/L_{25\mu\text{m}})$  at increasing  $\text{EW}_{11.3\mu\text{mPAH}}$ , which indicates that the rest-frame IR color  $\log(L_{60\mu\text{m}}/L_{25\mu\text{m}})$  is to the first order driven by the relative brightness of star-forming regions and the dusty tori. A relationship between IR color  $f_{30\mu\text{m}}/f_{15\mu\text{m}}$  and  $\text{EW}_{7.7\mu\text{mPAH}}$  is also observed in the sample of Veilleux et al. (2009) that is composed of PG quasars and ULIRGs. However, such correlations are not always observed in other samples of galaxies and AGN (Wu et al. 2010; Stierwalt et al. 2013). Wu et al. (2010) investigated the IR SEDs of about 300 galaxies and AGN selected to be brighter than 5 mJy at  $24\mu\text{m}$ . They found their objects are divided into two categories, one with low  $\text{EW}_{6.2\mu\text{mPAH}}$  and  $\log(f_{70\mu\text{m}}/f_{24\mu\text{m}})$ , and another with high  $\text{EW}_{6.2\mu\text{mPAH}}$  and  $\log(f_{70\mu\text{m}}/f_{24\mu\text{m}})$  but with no apparent correlation between  $\text{EW}_{6.2\mu\text{mPAH}}$  and  $\log(f_{70\mu\text{m}}/f_{24\mu\text{m}})$  within the category. Stierwalt et al. (2013) mainly focused on the IR SEDs of LIRGs and did not see a relationship between  $f_{30\mu\text{m}}/f_{15\mu\text{m}}$  and  $\text{EW}_{6.2\mu\text{mPAH}}$  either. As mentioned by Stierwalt et al. (2013), the IR slope is not only affected by the star-forming contribution but is also affected by the obscuration, which could cause a steep IR spectrum even at low  $\text{EW}_{\text{PAH}}$  if the energy source is heavily buried. Our quasar samples lack heavily buried sources, as indicated by the distributions of the silicate feature in Figure 7.

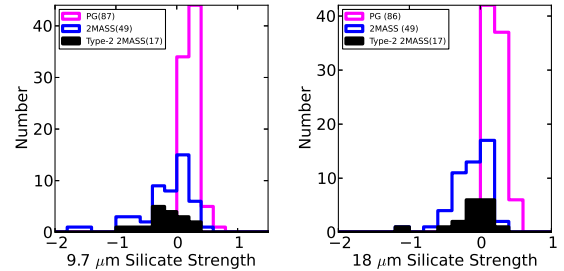


FIG. 7.— The distributions of silicate feature strengths for PG and 2MASS quasars. The  $9.7\mu\text{m}$  feature is shown in the left panel and the  $18\mu\text{m}$  feature is in the right panel.

The mid-IR slope is then mainly driven by the star-forming contribution and thus shows a correlation with the  $\text{EW}_{\text{PAH}}$ .

We further investigated the star-forming contribution at individual wavelengths (25 or  $60\mu\text{m}$ ) and their trend with the  $\text{EW}_{\text{PAH}}$ . As shown in the middle panel of Figure 6, the star-forming fraction at rest-frame  $25\mu\text{m}$  is usually below 30%, indicating the emission at this wavelength is generally dominated by the radiation from the dusty torus. This fraction is correlated with the  $\text{EW}_{11.3\mu\text{mPAH}}$ , as might be expected because the SF is not the dominant contributor, and both the quasar and star-forming SEDs do not change significantly from source to source. On the other hand, as shown in the right panel of Figure 6, the rest-frame  $60\mu\text{m}$  radiation is dominated by star formation, with the star-forming fraction mostly above 30%. This fraction does not show an apparent relation with the  $\text{EW}_{11.3\mu\text{mPAH}}$ , again as might be expected since the two indicators are mainly affected by different processes, SF dominating the  $60\mu\text{m}$  while  $\text{EW}_{11.3\mu\text{mPAH}}$  is a measure of the fraction of the output at this wavelength due to star formation to that from nuclear accretion, since the latter dominates the  $11.3\mu\text{m}$  continuum.

#### 4.3. Silicate Features

Figure 7 shows the distributions of the  $9.7$  and  $18\mu\text{m}$  silicate feature strengths including non-detections. The non-detected features are weak with  $3\text{-}\sigma$  upper limits for  $\ln(f_{\text{peak}}/f_{\text{cont}}^{\text{peak}})$  between -0.3 and 0.3. As shown in the figure, PG quasars mainly show emission features while the majority of 2MASS quasars have fea-

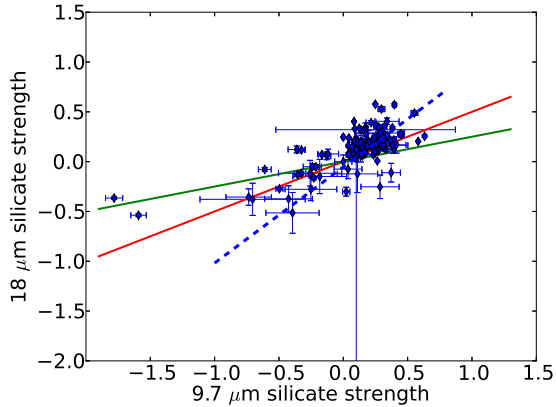


FIG. 8.— The  $18\ \mu\text{m}$  silicate feature strength vs.  $9.7\ \mu\text{m}$  feature strength. Symbols indicate the measurements of PG and 2MASS objects where the dashed line is the best linear fit. The red and green areas are the predictions for clumpy and smooth dusty tori, respectively (Feltre et al. 2012).

tures in absorption, which is consistent with the expectations from the unified model where the dusty tori of the unobscured quasars are viewed face-on and those of obscured quasars are seen edge-on. However, there is no good relation between the silicate feature and quasar optical type; e.g., many type 2 quasars show silicate features in emission. As indicated in the figure, the feature strength is moderate, with the majority in the range of  $\ln(f^{\text{peak}}/f_{\text{cont}}^{\text{peak}}) = -0.5$  to  $0.5$ . The lack of strong ( $>0.5$  or  $<-0.5$ )  $9.7\ \mu\text{m}$  silicate emission features is consistent with expectations if the dusty torus is clumpy instead of smooth (Fritz et al. 2006; Hönig et al. 2006; Nenkov et al. 2008; Schartmann et al. 2008; Stalevski et al. 2012; Feltre et al. 2012).

Figure 8 shows the relationship between two silicate feature strengths for sources with  $\text{EW}_{11.3\mu\text{mPAH}} < 0.2$ . The two features are roughly correlated, with a Pearson value of 0.6. A regression fit to the data points gives  $S_{18\mu\text{m}} = 0.96S_{9.7\mu\text{m}} - 0.05$  and  $1\text{-}\sigma$  scatter of 0.83. The relatively large scatter partly arises from the uncertainties in determining the underlying continuum. As shown in Figure 7, the small dynamic range of the two feature strengths will also limit the accuracy in the slope measurement. In Figure 8, we overlay some predictions of clumpy and smooth models (Feltre et al. 2012). The clumpy model produces a slope closer to the observations than the smooth model. In a dust geometry composed of clumps, the sides of individual clouds facing the central nuclei are heated and produce silicate emission features while the absorption features are imposed on the output from the dark sides. In an inclined viewing angle toward the AGN, the foreground clouds partially block the view of the background ones. Therefore, a majority of clouds are viewed from the dark sides and silicate absorption features dominate, although some fraction of clouds are seen from their bright sides and the associated silicate emission reduces the strength of the absorption trough. As the  $9.7\ \mu\text{m}$  feature has a larger optical depth than the  $18\ \mu\text{m}$  one, implying a stronger emission feature at  $9.7\ \mu\text{m}$  from the bright side of the cloud, the  $9.7\ \mu\text{m}$  absorption feature is reduced more so that a steeper slope is produced.

Figure 9 shows the distribution of the peak wavelengths of  $9.7\ \mu\text{m}$  features with  $\text{S/N} > 5$ . Almost all “ $9.7$

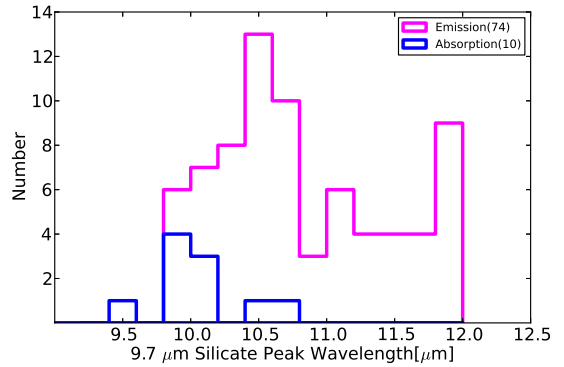


FIG. 9.— The distribution of the peak wavelength of the “ $9.7\ \mu\text{m}$ ” silicate feature for all cases with  $\text{S/N} > 5$ .

μm” features peak in emission at wavelengths longer than  $9.7\ \mu\text{m}$ , the peak location of silicate features observed in Galactic sources or star-forming galaxies (Smith et al. 2010). Some of them even peak at the longest wavelength ( $12\ \mu\text{m}$ ) that is allowed by our fit, indicating that they could peak at even longer wavelength. In contrast, those in absorption show minima at the expected  $9.7\ \mu\text{m}$  wavelength. The offsets in the peak wavelengths of emission features in quasars have been observed previously in small samples (Siebenmorgen et al. 2005; Hao et al. 2005; Sturm et al. 2005, 2006; Shi et al. 2006). None of the existing dusty torus models that adopt Milky Way ISM dust composition predict such offsets (Fritz et al. 2006; Hönig et al. 2006; Nenkov et al. 2008; Schartmann et al. 2008; Stalevski et al. 2012; Feltre et al. 2012). We have used the library of embedded young stellar object SEDs from Whitney (2014) to test whether the offset could arise from radiative transfer effects, but find that our fitting procedure generally centers the silicate features near  $9.7\ \mu\text{m}$  for them. We conclude that the offset is intrinsic to the quasars. Such differences between silicate absorption and emission features likely indicate that the physical properties of the emitting dust grains are subject to modifications due to exposure to the strong nuclear radiation, while “normal” dust grains in the host galaxies or outer cold edges of the dusty tori are responsible for the absorption features. It has been shown that for individual cases, the silicate emission feature in quasars can be well reproduced by adopting large size dust grains or modifying the dust compositions (Molster & Waters 2003; Smith et al. 2010).

Figure 10 shows the  $9.7\ \mu\text{m}$  silicate feature strength vs. the EW of the  $11.3\ \mu\text{m}$  aromatic feature. No relationship between the two is observed, which is also seen in other AGN samples (Hernán-Caballero et al. 2011). Unlike LIRGs and ULIRGs (Spoon et al. 2007; Stierwalt et al. 2013), our quasar sample does not show any deep silicate features (strength  $< -1.5$ ) at any  $\text{EW}_{11.3\mu\text{mPAH}}$ , while LIRGs and ULIRGs contain a branch in this plane that shows deeper silicate features at decreasing  $\text{EW}_{11.3\mu\text{mPAH}}$ , pointing to a population of deeply buried sources.

## 5. CONCLUSIONS

We report mid-infrared spectroscopy and mid- and far-infrared photometry of the PG and 2MASS samples of quasars. We analyze these data by fitting for spectral



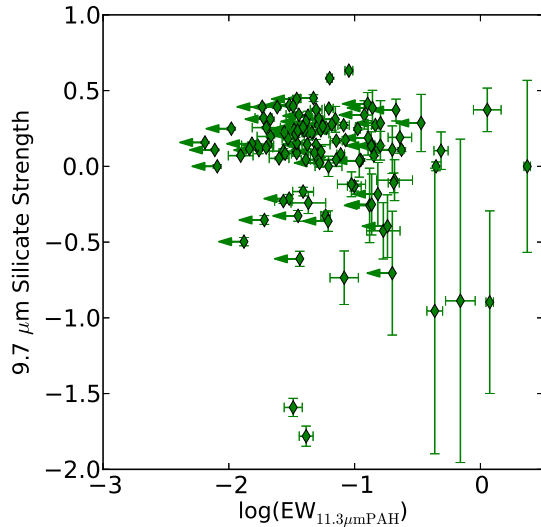


FIG. 10.— The  $9.7\ \mu\text{m}$  silicate feature strength as a function of the  $11.3\ \mu\text{m}$  aromatic feature equivalent width.

features due to aromatics and silicates. The broadband

infrared SEDs of both quasar types are similar. However, the PG quasars tend to have silicates in emission and the 2MASS ones have them in absorption. We show that the star formation rates estimated from the aromatic features and the far infrared luminosities of these quasars are consistent. Emission due to star formation in the host galaxies dominates the outputs of these systems at  $160\ \mu\text{m}$ , but at  $70\ \mu\text{m}$  and low SFRs it is likely that the quasar contaminates the star-forming SED significantly. The peak wavelength of the ' $10\ \mu\text{m}$ ' silicate feature tends to be longer than observed in the general interstellar medium, suggesting that the grain properties are modified by proximity to the AGNs.

## 6. ACKNOWLEDGMENT

We thank the anonymous referee for helpful comments that improve the paper significantly. Y.S. acknowledges support for this work from Natural Science Foundation of China under the grant of 11373021 and by the Strategic Priority Research Program "The Emergence of Cosmological Structures" of the Chinese Academy of Sciences, Grant No. XDB09000000.

## REFERENCES

- Antonucci, R. 1993, *ARA&A*, 31, 473
- Balog, Z., Müller, T., Nielbock, M., et al. 2013, *Experimental Astronomy*, 38
- Boroson, T. A., & Green, R. F. 1992, *ApJS*, 80, 109
- Calzetti, D., Kennicutt, R. C., Engelbracht, C. W., et al. 2007, *ApJ*, 666, 870
- Cutri, R. M., et al. 2001, *ASP Conf. Ser.* 232: The New Era of Wide Field Astronomy, 232, 78
- Diamond-Stanic, A. M., Rieke, G. H., & Rigby, J. R. 2009, *ApJ*, 698, 623
- Diamond-Stanic, A. M., & Rieke, G. H. 2010, *ApJ*, 724, 140
- Elvis, M., Wilkes, B. J., McDowell, J. C., et al. 1994, *ApJS*, 95, 1
- Esquej, P., Alonso-Herrero, A., González-Martín, O., et al. 2014, *ApJ*, 780, 86
- Feltre, A., Hatziminaoglou, E., Fritz, J., & Franceschini, A. 2012, *MNRAS*, 426, 120
- Ferrarese, L., & Merritt, D. 2000, *ApJ*, 539, L9
- Fritz, J., Franceschini, A., & Hatziminaoglou, E. 2006, *MNRAS*, 366, 767
- Gebhardt, K., et al. 2000, *ApJ*, 539, L13
- Gordon, K. D., Rieke, G. H., Engelbracht, C. W., et al. 2005, *PASP*, 117, 503
- Goldschmidt, P., Miller, L., La Franca, F., & Cristiani, S. 1992, *MNRAS*, 256, 65P
- Hao, L., Spoon, H. W. W., Sloan, G. C., et al. 2005, *ApJ*, 625, L75
- Hernán-Caballero, A., Pérez-Fournon, I., Hatziminaoglou, E., et al. 2009, *MNRAS*, 395, 1695
- Hernán-Caballero, A., Hatziminaoglou, E. 2011, *MNRAS*, 414, 500
- Hiner, K. D., Canalizo, G., Lacy, M., et al. 2009, *ApJ*, 706, 508
- Hönig, S. F., Beckert, T., Ohnaka, K., & Weigelt, G. 2006, *A&A*, 452, 459
- Jaffe, W., Meisenheimer, K., Röttgering, H. J. A., et al. 2004, *Nature*, 429, 47
- Jester, S., et al. 2005, *AJ*, 130, 873
- Kellermann, K. I., Sramek, R., Schmidt, M., Shaffer, D. B., & Green, R. 1989, *AJ*, 98, 1195
- Kormendy, J., & Richstone, D. 1995, *ARA&A*, 33, 581
- Lutz, D., Sturm, E., Tacconi, L. J., et al. 2008, *ApJ*, 684, 853
- Magorrian, J., et al. 1998, *AJ*, 115, 2285
- Molster, F. J., & Waters, L. B. F. M. 2003, *Astrophysical Journal*, 609, 121
- Nenkova, M., Sirocky, M. M., Nikutta, R., Ivezić, Ž., & Elitzur, M. 2008, *ApJ*, 685, 160
- Netzer, H., Lutz, D., Schweitzer, M., et al. 2007, *ApJ*, 666, 806
- Peeters, E., Spoon, H. W. W., & Tielens, A. G. G. M. 2004, *ApJ*, 613, 986
- Rieke, G. H., Alonso-Herrero, A., Weiner, B. J., et al. 2009, *ApJ*, 692, 556
- Richards, G. T., Lacy, M., Storrie-Lombardi, L. J., et al. 2006, *ApJS*, 166, 470
- Rosario, D. J., Trakhtenbrot, B., Lutz, D., et al. 2013, *A&A*, 560, A72
- Schartmann, M., Meisenheimer, K., Camenzind, M., et al. 2008, *A&A*, 482, 67
- Schmidt, M., & Green, R. F. 1983, *ApJ*, 269, 352
- Shang, Z., Brotherton, M. S., Wills, B. J., et al. 2011, *ApJS*, 196, 2
- Shi, Y., Rieke, G. H., Hines, D. C., et al. 2006, *ApJ*, 653, 127
- Shi, Y., Ogle, P., Rieke, G. H., et al. 2007, *ApJ*, 669, 841
- Siebenmorgen, R., Haas, M., Krügel, E., & Schulz, B. 2005, *A&A*, 436, L5
- Smith, P. S., Schmidt, G. D., Hines, D. C., Cutri, R. M., & Nelson, B. O. 2002, *ApJ*, 569, 23
- Smith, H. A., Li, A., Li, M. P., et al. 2010, *ApJ*, 716, 490
- Smith, J. D. T., et al. 2007, *ApJ*, 656, 770
- Spoon, H. W. W., Marshall, J. A., Houck, J. R., et al. 2007, *ApJ*, 654, L49
- Stalevski, M., Fritz, J., Baes, M., Nakos, T., & Popović, L. Č. 2012, *MNRAS*, 420, 2756
- Stierwalt, S., Armus, L., Surace, J. A., et al. 2013, *ApJS*, 206, 1
- Sturm, E., Hasinger, G., Lehmann, I., et al. 2006, *ApJ*, 642, 81
- Sturm, E., Schweitzer, M., Lutz, D., et al. 2005, *ApJ*, 629, L21
- Vega, O., Bressan, A., Panuzzo, P., et al. 2010, *ApJ*, 721, 1090
- Veilleux, S., Rupke, D. S. N., Kim, D.-C., et al. 2009, *ApJS*, 182, 628
- Whitney, B. 2014, <http://caravan.astro.wisc.edu/protostars/>
- Wu, Y., Helou, G., Armus, L., et al. 2010, *ApJ*, 723, 895

TABLE 1  
PHYSICAL PROPERTIES OF OUR SAMPLE

Number (1)	Name (2)	Position(J2000) (3)	$z$ (4)	$m_B$ (5)	$m_K$ (6)	Type (7)
1	PG0003+158	00h05m59.24s +16d09m49.0s	0.450	15.960		1.0
2	PG0003+199	00h06m19.52s +20d12m10.5s	0.025	13.750		1.0
3	PG0007+106	00h10m31.01s +10d58m29.5s	0.089	16.110		1.0
4	PG0026+129	00h29m13.60s +13d16m03.0s	0.142	14.950		1.0
5	PG0043+039	00h45m47.27s +04d10m24.4s	0.384	15.880		1.0
6	PG0049+171	00h51m54.80s +17d25m58.4s	0.064	15.880		1.0
7	PG0050+124	00h53m34.94s +12d41m36.2s	0.061	14.390		1.0
8	PG0052+251	00h54m52.10s +25d25m38.0s	0.155	15.420		1.0
9	PG0157+001	01h59m50.21s +00d23m40.6s	0.164	15.200		1.0
10	PG0804+761	08h10m58.60s +76d02m42.0s	0.100	15.150		1.0
11	PG0838+770	08h44m45.26s +76d53m09.5s	0.131	16.300		1.0
12	PG0844+349	08h47m42.47s +34d45m04.4s	0.064	14.000		1.0
13	PG0921+525	09h25m12.87s +52d17m10.5s	0.035	15.620		1.0
14	PG0923+201	09h25m54.72s +19d54m05.1s	0.190	16.040		1.0
15	PG0923+129	09h26m03.29s +12d44m03.6s	0.029	14.930		1.0
16	PG0934+013	09h37m01.03s +01d05m43.5s	0.050	16.290		1.0
17	PG0947+396	09h50m48.39s +39d26m50.5s	0.206	16.400		1.0
18	PG0953+414	09h56m52.39s +41d15m22.3s	0.239	15.050		1.0
19	PG1001+054	10h04m20.14s +05d13m00.5s	0.161	16.130		1.0
20	PG1004+130	10h07m26.10s +12d48m56.2s	0.240	15.930		1.0
21	PG1011-040	10h14m20.69s -04d18m40.5s	0.058	15.490		1.0
22	PG1012+008	10h14m54.90s +00d33m37.4s	0.185	15.890		1.0
23	PG1022+519	10h25m31.28s +51d40m34.9s	0.045	16.120		1.0
24	PG1048+342	10h51m43.90s +33d59m26.7s	0.167	15.810		1.0
25	PG1048-090	10h51m29.90s -09d18m10.0s	0.344	16.000		1.0
26	PG1049-005	10h51m51.44s -00d51m17.7s	0.357	15.950		1.0
27	PG1100+772	11h04m13.69s +76d58m58.0s	0.313	15.860		1.0
28	PG1103-006	11h06m31.77s -00d52m52.5s	0.425	16.020		1.0
29	PG1114+445	11h17m06.40s +44d13m33.3s	0.144	16.050		1.0
30	PG1115+407	11h18m30.29s +40d25m54.0s	0.154	16.020		1.0
31	PG1116+215	11h19m08.68s +21d19m18.0s	0.177	15.170		1.0
32	PG1119+120	11h21m47.10s +11d44m18.3s	0.049	14.650		1.0
33	PG1121+422	11h24m39.18s +42d01m45.0s	0.234	16.020		1.0
34	PG1126-041	11h29m16.66s -04d24m07.6s	0.060	15.430		1.0
35	PG1149-110	11h52m03.54s -11d22m24.3s	0.049	15.460		1.0
36	PG1151+117	11h53m49.27s +11d28m30.4s	0.176	15.510		1.0
37	PG1202+281	12h04m42.11s +27d54m11.8s	0.165	15.020		1.0
38	PG1211+143	12h14m17.70s +14d03m12.6s	0.085	14.630		1.0
39	PG1216+069	12h19m20.93s +06d38m38.5s	0.334	15.680		1.0
40	PG1226+023	12h29m06.70s +02d03m08.6s	0.158	12.860		1.0
41	PG1229+204	12h32m03.60s +20d09m29.2s	0.064	14.650		1.0
42	PG1244+026	12h46m35.25s +02d22m08.8s	0.048	16.150		1.0
43	PG1259+593	13h01m12.93s +59d02m06.7s	0.472	15.600		1.0
44	PG1302-102	13h05m33.01s -10d33m19.4s	0.286	15.090		1.0
45	PG1307+085	13h09m47.00s +08d19m48.2s	0.155	15.280		1.0
46	PG1309+355	13h12m17.77s +35d15m21.2s	0.184	15.450		1.0
47	PG1310-108	13h13m05.78s -11d07m42.4s	0.035	15.550		1.0
48	PG1322+659	13h23m49.52s +65d41m48.2s	0.168	15.860		1.0
49	PG1341+258	13h43m56.75s +25d38m47.7s	0.087	15.930		1.0
50	PG1351+236	13h54m06.43s +23d25m49.1s	0.055	15.870		1.0
51	PG1351+640	13h53m15.83s +63d45m45.7s	0.087	15.420		1.0
52	PG1352+183	13h54m35.69s +18d05m17.5s	0.158	15.710		1.0
53	PG1354+213	13h56m32.80s +21d03m52.4s	0.300	15.850		1.0
54	PG1402+261	14h05m16.21s +25d55m34.1s	0.164	15.570		1.0
55	PG1404+226	14h06m21.89s +22d23m46.6s	0.098	15.820		1.0
56	PG1411+442	14h13m48.33s +44d00m14.0s	0.089	14.990		1.0
57	PG1415+451	14h17m00.70s +44d56m06.0s	0.114	15.740		1.0
58	PG1416-129	14h19m03.80s -13d10m44.0s	0.129	15.400		1.0
59	PG1425+267	14h27m35.61s +26d32m14.5s	0.366	15.670		1.0
60	PG1426+015	14h29m06.59s +01d17m06.5s	0.086	15.050		1.0
61	PG1427+480	14h29m43.07s +47d47m26.2s	0.221	16.330		1.0
62	PG1435-067	14h38m16.16s -06d58m21.3s	0.129	15.540		1.0
63	PG1440+356	14h42m07.46s +35d26m22.9s	0.077	15.000		1.0
64	PG1444+407	14h46m45.94s +40d35m05.8s	0.267	15.950		1.0
65	PG1448+273	14h51m08.76s +27d09m26.9s	0.065	15.010		1.0
66	PG1501+106	15h04m01.20s +10d26m16.2s	0.036	15.090		1.0
67	PG1512+370	15h14m43.04s +36d50m50.4s	0.371	15.970		1.0
68	PG1519+226	15h21m14.26s +22d27m43.9s	0.137	16.090		1.0
69	PG1534+580	15h35m52.36s +57d54m09.2s	0.030	15.540		1.0
70	PG1535+547	15h36m38.36s +54d33m33.2s	0.038	15.310		1.0
71	PG1543+489	15h45m30.24s +48d46m09.1s	0.400	16.050		1.0
72	PG1545+210	15h47m43.54s +20d52m16.6s	0.266	16.050		1.0
73	PG1552+085	15h54m44.58s +08d22m21.5s	0.119	16.020		1.0
74	PG1612+261	16h14m13.20s +26d04m16.2s	0.131	16.000		1.0
75	PG1613+658	16h13m57.18s +65d43m09.6s	0.129	15.370		1.0

TABLE 1  
PHYSICAL PROPERTIES OF OUR SAMPLE

76	PG1617+175	16h20m11.29s +17d24m27.7s	0.114	15.530	1.0
77	PG1626+554	16h27m56.12s +55d22m31.5s	0.133	16.170	1.0
78	PG1700+518	17h01m24.80s +51d49m20.0s	0.282	15.430	1.0
79	PG1704+608	17h04m41.38s +60d44m30.5s	0.371	15.900	1.0
80	PG2112+059	21h14m52.57s +06d07m42.5s	0.466	15.520	1.0
81	PG2130+099	21h32m27.81s +10d08m19.5s	0.061	14.620	1.0
82	PG2209+184	22h11m53.89s +18d41m49.9s	0.070	15.860	1.0
83	PG2214+139	22h17m12.26s +14d14m20.9s	0.067	14.980	1.0
84	PG2233+134	22h36m07.68s +13d43m55.3s	0.325	16.040	1.0
85	PG2251+113	22h54m10.40s +11d36m38.3s	0.323	16.250	1.0
86	PG2304+042	23h07m02.91s +04d32m57.2s	0.042	15.440	1.0
87	PG2308+098	23h11m17.76s +10d08m15.5s	0.432	16.120	1.0
88	2MASSJ000703.6+155423	00h07m03.60s +15d54m23.8s	0.114	13.100	1.8
89	2MASSJ000810.8+135452	00h08m10.86s +13d54m52.3s	0.185	14.400	2.0
90	2MASSJ004118.7+281640	00h41m18.70s +28d16m40.0s	0.194	12.500	1.0
91	2MASSJ005010.1+280619	00h50m10.05s +28d06m20.7s	0.277	15.130	
92	2MASSJ005055.7+293328	00h50m55.70s +29d33m28.1s	0.136	13.220	2.0
93	2MASSJ010230.1+262337	01h02m30.10s +26d23m37.0s	0.194	13.830	1.0
94	2MASSJ010835.1+214818	01h08m35.10s +21d48m18.0s	0.285	13.460	1.9
95	2MASSJ012031.5+200327	01h20m31.50s +20d03m27.0s	0.087	12.470	
96	2MASSJ015721.0+171248	01h57m21.00s +17d12m48.0s	0.213	13.160	1.0
97	2MASSJ022150.6+132741	02h21m50.60s +13d27m40.8s	0.140	13.250	1.8
98	2MASSJ024807.3+145957	02h48m07.36s +14d59m57.7s	0.072	12.650	1.0
99	2MASSJ034857.6+125547	03h48m57.68s +12d55m47.4s	0.210	13.600	1.0
100	2MASSJ081652.2+425829	08h16m52.24s +42d58m29.4s	0.235	13.730	1.0
101	2MASSJ082311.3+435318	08h23m11.27s +43d53m18.5s	0.182	12.850	1.5
102	2MASSJ091848.6+211717	09h18m48.61s +21d17m17.0s	0.149	12.550	1.5
103	2MASSJ092049.0+190320	09h20m49.00s +19d03m20.0s	0.156	14.920	1.0
104	2MASSJ094636.4+205610	09h46m36.43s +20d56m11.0s	0.280	13.720	1.5
105	2MASSJ095504.5+170556	09h55m04.55s +17d05m56.4s	0.139	13.440	1.0
106	2MASSJ100121.1+215011	10h01m21.17s +21d50m11.2s	0.248	14.680	
107	2MASSJ101400.4+194614	10h13m58.99s +19d45m59.1s	0.110	12.370	1.5
108	2MASSJ101649.3+215435	10h16m49.35s +21d54m35.0s	0.257	13.940	1.0
109	2MASSJ102724.9+121920	10h27m24.98s +12d19m19.8s	0.231	13.220	1.5
110	2MASSJ105144.2+353930	10h51m44.24s +35d39m30.8s	0.158	13.540	
111	2MASSJ125807.4+232921	12h58m07.46s +23d29m21.6s	0.259	13.450	1.0
112	2MASSJ130005.3+163214	13h00m05.35s +16d32m14.8s	0.080	11.860	1.0
113	2MASSJ130700.6+233805	13h07m00.63s +23d38m05.2s	0.275	13.450	1.0
114	2MASSJ132917.5+121340	13h29m17.52s +12d13m40.2s	0.203	14.120	1.0
115	2MASSJ134915.2+220032	13h49m15.20s +22d00m32.7s	0.062	12.240	1.5
116	2MASSJ1402511+263117	14h02m51.20s +26d31m17.6s	0.187	12.670	1.0
117	2MASSJ145331.5+135358	14h53m31.52s +13d53m58.7s	0.139	13.090	1.0
118	2MASSJ145406.6+195028	14h54m06.68s +19d50m28.2s	0.260	14.710	1.5
119	2MASSJ145410.1+195648	14h54m10.17s +19d56m48.7s	0.243	14.170	1.9
120	2MASSJ145608.6+275008	14h56m08.65s +27d50m08.8s	0.250	13.380	1.0
121	2MASSJ150113.1+232908	15h01m13.20s +23d29m08.3s	0.258	13.460	1.0
122	2MASSJ151621.1+225944	15h16m21.11s +22d59m44.7s	0.190	14.120	1.0
123	2MASSJ151653.2+190048	15h16m53.23s +19d00m48.3s	0.190	11.410	1.0
124	2MASSJ151901.5+183804	15h19m01.48s +18d38m04.9s	0.187	14.250	1.0
125	2MASSJ152151.0+225120	15h21m51.00s +22d51m20.0s	0.287	14.300	1.0
126	2MASSJ154307.7+193751	15h43m07.78s +19d37m51.8s	0.228	12.740	1.5
127	2MASSJ163700.2+222114	16h37m00.22s +22d21m14.1s	0.211	13.590	1.0
128	2MASSJ163736.5+254302	16h37m36.52s +25d43m02.8s	0.277	14.170	1.9
129	2MASSJ165939.7+183436	16h59m39.77s +18d34m36.8s	0.170	12.910	1.5
130	2MASSJ170536.6+210137	17h05m36.66s +21d01m38.0s	0.271	14.310	1.0
131	2MASSJ171442.7+260248	17h14m42.77s +26d02m48.6s	0.163	13.080	1.0
132	2MASSJ222221.1+195947	22h22m21.14s +19d59m47.1s	0.211	12.920	1.0
133	2MASSJ222554.2+195837	22h25m54.25s +19d58m37.2s	0.147	13.490	2.0
134	2MASSJ223742.6+145614	22h37m42.60s +14d56m14.0s	0.277	14.000	1.0
135	2MASSJ223946.0+192955	22h39m46.00s +19d29m55.0s	0.194	14.670	
136	2MASSJ230304.3+162440	23h03m04.30s +16d24m40.0s	0.289	14.670	2.0
137	2MASSJ230442.4+270616	23h04m42.40s +27d06m16.0s	0.237	14.770	1.5
138	2MASSJ234259.3+134750	23h42m59.36s +13d47m50.4s	0.299	14.190	1.5
139	2MASSJ234449.5+122143	23h44m49.56s +12d21m43.1s	0.199	12.910	1.0

NOTE. — Col. (2): the name of the target; Col. (3): the position of the target; Col. (4): redshift; Col. (5): B-band magnitude of PG quasars in Vega system (see Schmidt & Green 1983); Col. (6):  $K_s$  magnitude of 2MASS quasars in internal 2MASS magnitude system<sup>a</sup>. The complete version of this table is in the electronic edition of the Journal. Col. (7): The optical type of emission line where 1.0 for broad emission line, 2.0 for narrow emission line and values between 1.0 and 2.0 for intermediate types.

<sup>a</sup> [http://www.ipac.caltech.edu/2mass/releases/allsky/doc/sec6\\_4a.html](http://www.ipac.caltech.edu/2mass/releases/allsky/doc/sec6_4a.html)

TABLE 2  
BROAD-BAND PHOTOMETRY OF THE SAMPLE

Number	Name	$f_{\text{Spitzer}-24\mu\text{m}}$ [mJy]	$f_{\text{Spitzer}-70\mu\text{m}}$ [mJy]	$f_{\text{Spitzer}-160\mu\text{m}}$ [mJy]	$f_{\text{Herschel}-160\mu\text{m}}$ [mJy]	$C_{\text{IRS-LL}}^{\text{IRS-SL}}$	$C_{\text{IRS}}^{\text{MIPS}}$
(1)	(2)	(3)	(4)	(5)	(6)	(7)	(8)
1	PG0003+158	24.69±0.38	21.26±4.29	<115.88	<40.68	1.31	0.99
2	PG0003+199	-9.00±1.00	329.80±11.0		138.06±12.3		1.77
3	PG0007+106	139.90±0.29	210.80±9.31	194.40±49.1	260.19±14.8	1.00	0.92
4	PG0026+129	46.82±0.37	<33.67	<112.96		1.29	1.13
5	PG0043+039	27.08±0.41	38.53±7.63	<60.59	89.71±13.76	0.95	1.18
6	PG0049+171	17.46±0.49	<14.48	<163.63	<40.56	1.00	1.06
7	PG0050+124	953.40±0.48	2084.00±11.	1612.00±34.	1884.34±17.	0.96	1.06
8	PG0052+251	71.19±0.33	82.07±8.68	<150.31	155.53±16.2	0.98	0.99
9	PG0157+001	-9.00±1.00			1301.47±11.	1.01	1.35
10	PG0804+761	199.10±0.31	122.70±5.71	<68.58	50.07±13.64	0.95	0.99
11	PG0838+770	75.25±0.27	140.60±6.82	117.70±22.3	224.59±12.5	0.94	1.15
12	PG0844+349	98.72±0.37	100.90±6.75	163.80±28.3	239.90±14.5	0.93	1.15
13	PG0921+525	93.44±0.31	95.75±10.03		142.30±10.2	0.91	1.16
14	PG0923+201	54.05±0.41	50.00±4.82	<227.46	63.26±12.65	0.89	1.13
15	PG0923+129	242.50±0.43			1059.21±14.	0.94	1.11
16	PG0934+013	86.50±0.39	214.60±10.8		305.10±15.0	0.94	1.12
17	PG0947+396	50.11±0.36	107.80±9.89		189.65±10.8	0.89	1.09
18	PG0953+414	46.15±0.34	39.49±10.73	<95.10	69.89±12.99	0.98	1.08
19	PG1001+054	38.50±0.40	39.85±5.94	<89.45	56.30±10.60	0.87	1.13
20	PG1004+130	80.60±0.50	104.20±3.99	<119.74	82.72±15.23	1.00	1.10
21	PG1011-040	104.00±0.33	179.80±6.96	266.60±40.4	233.90±13.7	1.00	1.08
22	PG1012+008	57.18±0.72	93.63±7.90	175.60±31.1	104.81±17.1	1.00	1.07
23	PG1022+519	46.62±0.29	246.90±7.94		288.98±11.5	0.94	1.08
24	PG1048+342	26.97±0.36	62.60±10.17	133.10±18.2	160.10±13.1	1.06	1.14
25	PG1048-090	25.31±0.35	57.32±6.75		<56.84	1.20	1.23
26	PG1049-005	101.90±0.37	259.80±6.27	<77.58	170.00±12.5	1.00	1.03
27	PG1100+772	48.81±0.26	61.16±2.66	<154.62	90.04±16.89	1.00	1.07
28	PG1103-006	37.95±0.35	55.29±6.97	<143.80	49.97±10.70	1.00	1.16
29	PG1114+445	137.20±0.33	88.37±6.91	<60.59	<42.98	1.00	1.08
30	PG1115+407	44.98±0.32	189.60±7.34	267.30±23.9	303.31±11.7	1.00	1.11
31	PG1116+215	103.70±0.45	64.96±10.16	<81.10		1.05	0.93
32	PG1119+120	235.70±0.35	351.70±7.97	334.20±36.7	346.25±11.8	1.00	1.08
33	PG1121+422	14.50±0.34	<10.49	<71.47	<39.66	0.97	1.19
34	PG1126-041	261.90±0.49	495.20±10.5	349.90±49.7	451.76±13.3	1.75	1.05
35	PG1149-110	119.40±0.41	220.50±14.3		349.89±12.7	0.94	1.04
36	PG1151+117	32.28±0.41	36.19±5.75	<108.66	<33.61	1.06	1.16
37	PG1202+281	82.08±0.36	85.88±13.59		91.88±13.24	1.00	1.05
38	PG1211+143	250.90±0.39	139.80±8.98	<114.47	<41.63	1.02	0.99
39	PG1216+069	28.21±0.41	<22.52		<42.43	0.82	1.22
40	PG1226+023	592.50±0.39	985.90±8.64	1010.00±26.		0.98	0.95
41	PG1229+204	155.50±0.34	152.40±6.64	198.60±31.1	250.75±12.1	1.00	1.15
42	PG1244+026	108.90±0.40	192.80±9.34	235.80±35.9	109.60±12.4	0.95	1.11
43	PG1259+593	22.29±0.28	22.94±3.86	<48.54	<41.71	0.97	1.07
44	PG1302-102	99.66±0.37	121.10±8.30	<136.95	184.77±13.8	0.95	1.09
45	PG1307+085	70.81±0.35	86.30±9.18	<107.19	63.89±11.51	1.00	0.97
46	PG1309+355	108.90±0.30	45.33±9.19	<56.05	132.10±13.9	1.22	0.98
47	PG1310-108	126.60±0.40	105.10±7.37	<128.36		0.93	1.12
48	PG1322+659	48.75±0.39	149.60±8.80	<87.11	136.28±14.9	0.97	1.13
49	PG1341+258	47.07±0.33	102.80±8.71		75.77±13.27	0.99	1.18
50	PG1351+236	53.75±0.37	369.80±7.64	375.60±21.2	491.88±11.7	1.01	0.98
51	PG1351+640	437.90±0.45	626.10±13.4	455.30±46.4	336.70±16.9	0.96	1.04
52	PG1352+183	32.28±0.34	18.18±4.84	<71.84	<39.22	5.37	1.05
53	PG1354+213	30.65±0.31	51.89±5.18	134.80±37.6	<40.59	1.04	1.12
54	PG1402+261	106.40±0.33	223.80±8.69	186.10±30.9	173.77±13.9	1.00	1.00
55	PG1404+226	27.96±0.33	47.12±5.98	<73.61	110.07±13.9	1.02	1.03
56	PG1411+442	123.80±0.28	140.80±6.12	94.89±16.63	179.71±15.3	1.14	1.07
57	PG1415+451	62.08±0.31	106.10±6.18	105.60±17.6	138.19±14.2	1.00	1.06
58	PG1416-129	28.26±0.38	29.88±6.43	<143.85	38.74±11.96	1.10	1.24
59	PG1425+267	49.08±0.30	82.70±2.71	<72.31	71.25±14.28	0.95	1.15
60	PG1426+015	189.90±0.37	301.90±9.89	298.60±32.2	344.06±13.9	0.95	1.12
61	PG1427+480	44.80±0.28	109.10±9.12	<66.01	51.73±10.71	1.09	1.11
62	PG1435-067	40.27±0.37	49.23±4.01	<84.19	<36.63	0.90	1.08
63	PG1440+356	184.90±0.31	807.10±10.1	597.50±31.1	628.43±16.6	0.95	1.11
64	PG1444+407	62.21±0.28	90.14±9.13	<95.16		0.99	1.04
65	PG1448+273	108.20±0.31	133.20±7.76	156.60±25.8	181.71±12.4	0.92	1.20
66	PG1501+106	433.50±0.41	365.00±8.96	135.40±18.6		1.01	1.02
67	PG1512+370	33.86±0.28	43.34±3.86	<68.37	64.35±11.06	0.98	1.17
68	PG1519+226	61.93±0.32	84.57±6.48	<107.36	88.82±11.01	0.96	1.05
69	PG1534+580	178.80±0.28	178.00±4.76	125.10±20.2		0.97	1.07
70	PG1535+547	77.58±0.29	96.20±5.91		114.81±15.4	1.07	1.16
71	PG1543+489	105.50±0.45	303.80±6.96	261.40±32.8	206.31±12.2	0.86	1.10
72	PG1545+210	35.84±0.29	37.85±2.13	<102.97	<38.30	1.04	1.01
73	PG1552+085	29.89±0.35	31.16±4.51	<58.00	<43.01	1.00	1.08



TABLE 2 — *Continued*

Number	Name	$f_{\text{Spitzer}-24\mu\text{m}}$ [mJy] (3)	$f_{\text{Spitzer}-70\mu\text{m}}$ [mJy] (4)	$f_{\text{Spitzer}-160\mu\text{m}}$ [mJy] (5)	$f_{\text{Herschel}-160\mu\text{m}}$ [mJy] (6)	$C_{\text{IRS-LL}}^{\text{IRS-SL}}$ (7)	$C_{\text{IRS}}^{\text{MIPS}}$ (8)
74	PG1612+261	99.88±0.34	211.90±6.71	121.60±39.7	229.89±14.4	0.93	1.09
75	PG1613+658	-9.00±1.00			793.21±16.1	0.95	1.51
76	PG1617+175	52.85±0.34	49.48±5.32	<93.83	<51.05	1.00	1.09
77	PG1626+554	18.69±0.30	21.22±5.40	<73.03		0.94	1.12
78	PG1700+518	188.10±0.26	401.30±4.72	207.30±27.0	328.60±12.3	1.11	1.07
79	PG1704+608	109.60±0.23	205.40±3.28	135.80±21.5	109.36±14.5	1.00	1.03
80	PG2112+059	76.31±0.31	68.78±6.19	<84.58	103.80±9.91	1.00	1.14
81	PG2130+099	312.60±0.32	486.30±6.98	330.10±25.1	397.25±12.0	1.05	1.00
82	PG2209+184	25.06±0.68	102.10±10.5	243.70±42.1	210.40±13.7	1.10	1.23
83	PG2214+139	98.17±0.33	103.50±8.46		136.31±10.1	0.98	1.13
84	PG2233+134	59.86±0.35	93.84±10.12	<177.06	85.11±10.14	0.94	1.10
85	PG2251+113	46.80±0.35	104.70±7.98	<114.14	77.57±13.83	0.95	1.08
86	PG2304+042	26.77±0.42	<29.95			1.07	1.02
87	PG2308+098	25.75±0.35	<30.94		<48.33	0.88	1.12
88	2MASSJ000703.6+155423	68.95±0.37	262.80±7.86	258.50±51.4		0.93	1.04
89	2MASSJ000810.8+135452	8.81±0.96	39.34±7.25	<186.76			
90	2MASSJ004118.7+281640	78.74±0.37	108.10±10.1	149.40±43.5		1.14	1.05
91	2MASSJ005010.1+280619	10.28±0.32	134.80±6.52	207.80±53.7		1.11	1.46
92	2MASSJ005055.7+293328	61.67±0.31	199.70±6.09	<83.01		1.11	1.04
93	2MASSJ010230.1+262337	18.27±0.32	33.31±7.11	<80.71		1.19	1.09
94	2MASSJ010835.1+214818	78.77±0.35	107.30±10.7	<128.46		1.09	1.04
95	2MASSJ012031.5+200327	7.50±0.39	92.06±8.82			0.87	2.25
96	2MASSJ015721.0+171248	33.50±0.36	240.30±14.3	<343.97		0.97	1.03
97	2MASSJ022150.6+132741	115.30±0.39	411.50±7.96	<179.55		1.82	1.03
98	2MASSJ024807.3+145957	84.15±0.43	177.60±9.95	<101.16		1.03	1.03
99	2MASSJ034857.6+125547	157.30±0.39	302.70±13.1	275.20±80.1		1.29	1.04
100	2MASSJ081652.2+425829	12.19±0.34	<11.89	<106.08		0.96	1.17
101	2MASSJ082311.3+435318	78.20±0.34	222.50±6.12	283.80±28.0		1.04	1.04
102	2MASSJ091848.6+211717	96.67±0.37	205.00±10.9	181.50±32.8		1.00	0.96
103	2MASSJ092049.0+190320	13.45±0.35	<23.70	<76.02		1.04	1.34
104	2MASSJ094636.4+205610	45.70±0.40	40.78±9.56	<121.49		1.06	1.05
105	2MASSJ095504.5+170556	20.95±0.41	16.25±4.97	<92.72		1.10	1.10
106	2MASSJ100121.1+215011	19.52±0.40	225.40±9.41	226.10±37.4		2.00	1.16
107	2MASSJ101400.4+194614	86.69±0.38	143.20±8.57				
108	2MASSJ101649.3+215435	23.37±0.39	42.89±7.75	<74.29		1.27	0.92
109	2MASSJ102724.9+121920	86.35±0.41	99.53±9.68			1.38	1.05
110	2MASSJ105144.2+353930	35.66±0.35	53.64±7.95			1.00	1.05
111	2MASSJ125807.4+232921	72.69±0.33	129.60±7.32	<84.02		1.02	0.96
112	2MASSJ130005.3+163214	162.50±0.37	68.99±7.36	<74.69		1.00	0.99
113	2MASSJ130700.6+233805	78.32±0.32	796.30±7.37	395.60±36.8		1.56	1.03
114	2MASSJ132917.5+121340	13.37±0.88	<30.72			1.26	1.23
115	2MASSJ134915.2+220032	200.10±0.35	413.40±6.19	227.40±31.7			
116	2MASSJ1402511+263117	26.99±0.29	29.89±4.37	<62.76		1.04	1.11
117	2MASSJ145331.5+135358	124.80±0.31	702.10±7.51	424.00±26.3		0.94	0.96
118	2MASSJ145406.6+195028	15.99±0.29	36.17±5.57	<79.24		1.32	1.13
119	2MASSJ145410.1+195648	32.34±0.32	38.69±6.66	<121.89		1.29	1.26
120	2MASSJ145608.6+275008	31.06±0.29	96.27±7.40	141.70±31.9		1.31	1.18
121	2MASSJ150113.1+232908	51.13±0.30	112.60±17.1	213.40±53.4		0.96	1.07
122	2MASSJ151621.1+225944	20.61±0.33	31.61±8.18	<130.20		1.25	1.06
123	2MASSJ151653.2+190048	135.80±0.31	82.47±9.66	95.02±27.06		1.02	0.98
124	2MASSJ151901.5+183804	10.44±0.31	22.44±2.57	<79.79		0.94	1.23
125	2MASSJ152151.0+225120	55.28±0.33	574.70±8.31	637.90±36.8		1.10	1.02
126	2MASSJ154307.7+193751	87.04±0.28	120.90±9.78	<79.39		1.03	1.02
127	2MASSJ163700.2+222114	25.44±0.67	146.30±14.7	255.80±30.9		1.17	0.42
128	2MASSJ163736.5+254302	40.33±0.25	86.63±7.84	<97.47		0.95	1.10
129	2MASSJ165939.7+183436	140.70±0.28	269.40±8.26			1.00	0.96
130	2MASSJ170536.6+210137	11.84±0.32	74.79±3.19	<111.69		0.90	1.05
131	2MASSJ171442.7+260248	26.09±0.32	75.63±3.35	<76.58		1.13	1.40
132	2MASSJ222221.1+195947	51.96±0.30	67.19±10.07			1.08	1.10
133	2MASSJ222554.2+195837	45.09±0.33	166.70±5.17	<113.14		0.92	1.00
134	2MASSJ223742.6+145614	20.75±0.33	91.35±7.19			1.14	1.14
135	2MASSJ223946.0+192955	7.61±0.30	70.38±6.57			0.87	2.12
136	2MASSJ230304.3+162440	4.66±0.33	104.50±8.25			0.88	1.00
137	2MASSJ230442.4+270616	5.63±0.33	33.15±6.39	<90.77		0.97	1.28
138	2MASSJ234259.3+134750	19.63±0.41	47.88±6.63	<93.73		1.13	1.15
139	2MASSJ234449.5+122143	59.40±0.35	152.60±8.76	<109.66		1.04	1.05

NOTE. — The factor in the column (7) is used to multiply with the IRS short-low to long-low, while the factor in the column (8) is used to scale the IRS to the MIPS 24  $\mu\text{m}$  photometry.

TABLE 3  
INFRARED SPECTRA AND PHOTOMETRY OF THE SAMPLE

Number	Name	wave	$f_\nu$	error
(1)	(2)	(3)	[mJy] (4)	[mJy] (5)
1	PG0003+158	5.52	7.01	0.43
		5.56	7.05	0.44
		5.59	6.95	0.31
		5.63	6.74	0.44
		5.67	6.98	0.42

NOTE. — The complete version of this table is in the electronic edition of the Journal.

TABLE 4  
MEASURED FEATURES AND PHYSICAL PARAMETERS

ID	Name	Str <sub>9.7μm-Sil</sub>	$\lambda_{9.7\mu\text{m-Sil}}^{\text{peak}}$ [μm]	Str <sub>18μm-Sil</sub>	$\lambda_{18\mu\text{m-Sil}}^{\text{peak}}$ [μm]	EW <sub>11.3μmPAH</sub> [μm]	LogL <sub>5μm</sub> [log(L <sub>⊙</sub> )]	LogL <sub>15μm</sub> [log(L <sub>⊙</sub> )]	LogL <sub>18μm</sub> [log(L <sub>⊙</sub> )]	LogL <sub>25μm</sub> [log(L <sub>⊙</sub> )]	log(SFR) [M <sub>⊙</sub> /yr]
1	PG0003+158	0.32±0.01	11.3	0.28±0.03	19.3	<0.032	11.81	11.74	11.78	11.63	1.43±0.30
2	PG0003+199	0.10±0.00	10.3			0.034±0.002	10.55	10.40	10.33	10.19	-0.94±0.30
3	PG0007+106	0.10±0.02	11.4	0.23±0.01	17.4	0.027±0.007	10.90	10.93	10.96	10.94	0.66±0.30
4	PG0026+129	0.30±0.02	10.1	0.30±0.02	17.8	<0.019	11.24	10.99	10.99	10.74	<0.65
5	PG0043+039	0.33±0.03	9.8	0.13±0.03	19.1	<0.043	11.75	11.62	11.66	11.58	1.64±0.30
6	PG0049+171	0.30±0.03	10.5	0.53±0.03	17.5	<0.041	10.05	9.92	9.92	9.61	<-0.65
7	PG0050+124	0.28±0.00	10.0	0.11±0.00	17.4	0.055±0.002	11.24	11.40	11.44	11.43	1.59±0.30
8	PG0052+251	0.22±0.04	10.5	0.39±0.02	17.4	0.046±0.014	11.19	11.22	11.24	10.99	1.05±0.30
9	PG0157+001	0.25±0.01	9.9	0.25±0.01	15.7	0.106±0.005	11.52	11.98	12.06	12.28	2.50±0.30
10	PG0804+761	0.32±0.01	10.0	0.14±0.00	20.2	0.019±0.003	11.43	11.23	11.25	11.13	-0.09±0.30
11	PG0838+770	0.09±0.02	10.2	0.15±0.01	17.3	0.035±0.007	10.86	11.03	11.06	11.02	1.01±0.30
12	PG0844+349	0.34±0.02	10.4	0.26±0.02	19.5	0.036±0.008	10.57	10.49	10.57	10.42	0.03±0.30
13	PG0921+525	0.25±0.01	10.9	0.58±0.01	17.7	<0.010	10.13	10.10	10.13	9.83	-0.63±0.30
14	PG0923+201	0.31±0.02	10.0	0.17±0.01	19.2	<0.028	11.49	11.26	11.26	11.14	1.06±0.30
15	PG0923+129	0.17±0.00	11.8	0.35±0.01	18.3	0.085±0.003	9.98	10.21	10.25	10.14	0.22±0.30
16	PG0934+013	0.08±0.01	11.1	0.15±0.01	18.2	0.077±0.005	10.03	10.18	10.23	10.21	0.16±0.30
17	PG0947+396	0.11±0.02	11.8	0.10±0.01	16.9	<0.017	11.38	11.30	11.30	11.23	1.39±0.30
18	PG0953+414	0.28±0.04	10.4	0.22±0.03	19.5	<0.052	11.65	11.42	11.42	11.25	1.29±0.30
19	PG1001+054	0.24±0.02	11.5	0.22±0.04	16.6	<0.033	11.16	10.95	10.96	10.87	0.55±0.30
20	PG1004+130	0.63±0.01	10.1	0.26±0.01	17.8	0.090±0.006	11.51	11.62	11.66	11.57	1.46±0.30
21	PG1011-040	0.38±0.01	10.7	0.34±0.01	18.1	0.062±0.005	10.27	10.44	10.49	10.37	0.23±0.30
22	PG1012+008	0.12±0.01	11.7	0.07±0.02	18.7	<0.021	11.26	11.26	11.26	11.21	1.26±0.30
23	PG1022+519	0.11±0.01	11.2	0.17±0.01	19.2	0.236±0.006	9.86	9.84	9.88	9.83	-0.03±0.30
24	PG1048+342	0.09±0.02	11.8	0.21±0.02	18.4	<0.031	10.89	10.88	10.88	10.71	1.05±0.30
25	PG1048-090	0.45±0.02	10.7	0.27±0.03	19.5	<0.047	11.62	11.48	11.49	11.41	1.55±0.30
26	PG1049-005	0.23±0.01	10.7	0.15±0.01	16.0	<0.013	12.04	12.11	12.14	12.15	2.17±0.30
27	PG1100+772	0.31±0.01	11.1	0.17±0.01	18.9	<0.021	11.75	11.70	11.70	11.62	1.64±0.30
28	PG1103-006	0.40±0.01	10.5	0.18±0.02	19.2	<0.030	11.88	11.89	11.89	11.81	1.76±0.30
29	PG1114+445	0.11±0.01	11.4	0.21±0.00	18.5	<0.008	11.36	11.41	11.43	11.28	0.60±0.50
30	PG1115+407	0.14±0.01	11.9	0.16±0.02	15.9	0.138±0.007	11.06	10.99	10.98	10.95	1.51±0.30
31	PG1116+215	0.27±0.06	10.8	0.20±0.02	19.5	<0.051	11.76	11.48	11.48	11.35	0.65±0.50
32	PG1119+120	0.15±0.01	11.8	0.18±0.01	16.6	0.035±0.005	10.35	10.63	10.65	10.62	0.18±0.30
33	PG1121+422	0.22±0.02	11.0	0.17±0.04	19.2	<0.043	11.28	10.93	10.90	10.69	<0.65
34	PG1126-041	-0.32±0.02	10.0	0.12±0.01	18.0	0.059±0.005	10.90	10.86	10.87	10.85	0.47±0.30
35	PG1149-110	0.14±0.01	11.4	0.32±0.01	17.6	0.017±0.005	10.04	10.32	10.37	10.31	0.20±0.30
36	PG1151+117	0.30±0.11	11.3	0.23±0.07	16.1	<0.225	11.11	10.99	10.99	10.85	0.39±0.50
37	PG1202+281	0.32±0.01	11.5	0.22±0.01	17.7	0.052±0.006	11.12	11.26	11.30	11.23	1.11±0.30
38	PG1211+143	0.18±0.01	10.4	0.20±0.00	19.5	0.030±0.003	11.20	11.19	11.22	11.07	0.32±0.50
39	PG1216+069	0.14±0.03	10.2	0.20±0.03	18.2	0.049±0.013	11.66	11.54	11.51	11.32	1.84±0.50
40	PG1226+023	0.11±0.00	10.4	0.15±0.00	19.6	<0.004	12.24	12.11	12.12	12.05	2.11±0.30
41	PG1229+204	0.25±0.02	10.8	0.36±0.01	18.4	0.059±0.010	10.58	10.66	10.74	10.64	0.19±0.30
42	PG1244+026	0.04±0.01	10.6	0.16±0.01	19.3	0.052±0.004	10.03	10.24	10.28	10.24	-0.06±0.30
43	PG1259+593	0.37±0.01	10.0	0.17±0.01	15.9	0.049±0.005	12.15	11.78	11.74	11.59	1.51±0.30
44	PG1302-102	0.29±0.01	10.9	0.19±0.01	16.4	<0.016	11.73	11.90	11.91	11.85	1.88±0.30
45	PG1307+085	0.34±0.09	10.1	0.40±0.03	19.2	<0.119	11.10	11.19	11.20	11.03	0.66±0.30
46	PG1309+355	0.31±0.09	10.7	0.22±0.02	19.5	<0.070	11.47	11.48	11.53	11.42	1.04±0.30
47	PG1310-108	0.08±0.01	10.7	0.40±0.01	18.7	0.028±0.003	9.93	10.17	10.21	9.96	-0.41±0.50
48	PG1322+659	0.20±0.01	11.4	0.20±0.01	17.9	0.021±0.005	11.19	11.08	11.10	11.03	1.36±0.30
49	PG1341+258	0.22±0.02	10.5	0.16±0.01	19.1	0.046±0.008	10.42	10.46	10.49	10.42	-0.03±0.30
50	PG1351+236	0.00±0.03	3.0	0.00±0.03	3.0	0.444±0.008	9.99	10.02	10.06	10.05	0.43±0.30
51	PG1351+640	0.58±0.01	10.0	0.20±0.00	17.0	0.063±0.003	11.06	11.31	11.42	11.39	1.32±0.30
52	PG1352+183	0.17±0.70	9.8	0.32±0.07	16.1	<0.969	11.23	10.87	10.87	10.73	-0.01±0.50
53	PG1354+213	0.13±0.01	10.8	0.15±0.03	15.9	<0.029	11.39	11.44	11.45	11.41	1.58±0.30

TABLE 4 — *Continued*

ID	Name	Str <sub>9.7μm-Sil</sub>	$\lambda_{9.7\mu\text{m-Sil}}^{\text{peak}}$ [μm]	Str <sub>18μm-Sil</sub>	$\lambda_{18\mu\text{m-Sil}}^{\text{peak}}$ [μm]	EW <sub>11.3μmPAH</sub> [μm]	Log <sub>L<sub>5μm</sub></sub> [log(L <sub>⊙</sub> )]	Log <sub>L<sub>15μm</sub></sub> [log(L <sub>⊙</sub> )]	Log <sub>L<sub>18μm</sub></sub> [log(L <sub>⊙</sub> )]	Log <sub>L<sub>25μm</sub></sub> [log(L <sub>⊙</sub> )]	log(SFR) [M <sub>⊙</sub> /yr]
54	PG1402+261	0.22±0.02	10.5	0.14±0.01	16.2	0.028±0.009	11.52	11.39	11.39	11.38	1.47±0.30
55	PG1404+226	0.27±0.02	10.2	0.19±0.02	17.7	0.082±0.008	10.41	10.39	10.40	10.29	0.40±0.30
56	PG1411+442	0.16±0.01	10.2	0.11±0.00	18.0	<0.006	11.36	10.99	10.97	10.83	0.15±0.30
57	PG1415+451	0.04±0.01	11.8	0.08±0.01	17.9	0.112±0.004	10.81	10.83	10.85	10.78	0.51±0.30
58	PG1416-129	0.55±0.03	11.8	0.49±0.02	16.7	<0.057	10.71	10.69	10.71	10.50	0.03±0.30
59	PG1425+267	0.15±0.01	10.6	0.06±0.01	16.3	<0.015	11.78	11.84	11.85	11.82	1.78±0.30
60	PG1426+015	0.23±0.01	10.6	0.22±0.00	17.1	0.035±0.004	11.08	11.10	11.11	11.00	1.06±0.30
61	PG1427+480	0.14±0.01	11.7	0.15±0.01	16.8	<0.021	11.18	11.27	11.30	11.34	1.10±0.30
62	PG1435-067	0.21±0.02	10.5	0.17±0.02	18.2	<0.034	10.91	10.83	10.82	10.64	0.25±0.50
63	PG1440+356	0.07±0.00	11.8	0.12±0.00	18.3	0.142±0.005	10.98	10.90	10.94	10.95	1.33±0.30
64	PG1444+407	0.23±0.01	10.2	0.07±0.01	18.6	0.040±0.004	11.62	11.64	11.65	11.57	1.50±0.30
65	PG1448+273	0.09±0.01	11.8	0.33±0.01	17.7	0.048±0.004	10.44	10.60	10.64	10.51	0.03±0.30
66	PG1501+106	0.00±0.01	3.0	0.25±0.00	18.5	<0.008	10.44	10.65	10.68	10.58	-0.63±0.30
67	PG1512+370	0.39±0.01	10.6	0.13±0.01	19.5	<0.018	11.70	11.70	11.70	11.63	1.66±0.30
68	PG1519+226	0.05±0.01	10.4	0.06±0.01	17.5	0.025±0.005	11.13	11.04	11.03	10.95	0.70±0.30
69	PG1534+580	0.12±0.00	11.1	0.33±0.00	18.0	0.020±0.002	9.97	10.12	10.16	10.02	-0.82±0.30
70	PG1535+547	0.12±0.01	10.6	0.19±0.01	18.4	0.015±0.003	10.29	10.07	10.05	9.86	-0.65±0.30
71	PG1543+489	0.26±0.01	11.8	0.13±0.01	15.6	<0.007	12.03	12.27	12.27	12.32	2.46±0.30
72	PG1545+210	0.28±0.04	11.6	0.34±0.03	19.1	<0.066	11.52	11.39	11.41	11.20	1.12±0.30
73	PG1552+085	0.24±0.01	10.4	0.16±0.02	15.6	0.035±0.007	10.74	10.64	10.60	10.48	-0.04±0.50
74	PG1612+261	0.04±0.01	11.8	0.24±0.01	17.1	0.041±0.003	11.01	11.15	11.19	11.16	1.02±0.30
75	PG1613+658	0.24±0.01	10.4	0.24±0.00	17.5	0.054±0.004	11.59	11.58	11.59	11.55	2.02±0.30
76	PG1617+175	0.26±0.02	10.1	0.11±0.01	18.9	<0.039	11.02	10.83	10.81	10.67	0.13±0.50
77	PG1626+554	0.44±0.02	10.3	0.28±0.01	19.6	<0.035	10.85	10.54	10.52	10.25	-0.09±0.50
78	PG1700+518	0.17±0.01	10.6	0.09±0.01	19.5	0.071±0.008	12.21	12.16	12.17	12.16	2.07±0.30
79	PG1704+608	0.39±0.01	10.7	0.22±0.01	17.3	<0.024	12.14	12.14	12.22	12.22	2.08±0.30
80	PG2112+059	0.26±0.01	10.2	0.01±0.01	18.6	0.056±0.004	12.41	12.29	12.28	12.21	2.08±0.30
81	PG2130+099	0.07±0.00	11.9	0.15±0.01	16.4	0.012±0.003	10.98	10.99	10.98	10.92	0.46±0.30
82	PG2209+184	0.27±0.02	10.4	0.27±0.09	17.6	0.146±0.010	10.29	10.12	10.11	9.91	0.45±0.30
83	PG2214+139	0.26±0.01	10.2	0.18±0.01	18.2	0.020±0.005	10.93	10.66	10.66	10.46	-0.01±0.30
84	PG2233+134	0.20±0.03	11.3	0.20±0.02	19.4	<0.049	11.65	11.75	11.82	11.74	1.78±0.30
85	PG2251+113	0.32±0.02	11.0	0.35±0.02	17.7	<0.027	11.79	11.71	11.70	11.54	1.67±0.30
86	PG2304+042	0.40±0.01	10.6	0.57±0.01	17.1	<0.032	9.70	9.75	9.75	9.45	<-0.81
87	PG2308+098	0.37±0.02	10.8	0.21±0.03	18.8	<0.033	11.88	11.74	11.73	11.59	<1.66
88	2MASSJ000703.6+155423	0.00±0.07	3.0	0.00±0.07	3.0	0.062±0.015	10.71	10.83	10.85	10.93	1.24±0.30
89	2MASSJ000810.8+135452										1.05±0.30
90	2MASSJ004118.7+281640	0.41±0.07	10.7	0.17±0.08	15.7	<0.127	11.53	11.45	11.43	11.40	1.45±0.30
91	2MASSJ005010.1+280619	0.00±0.57	3.0	0.00±0.57	3.0	2.357±0.141	10.66	10.66	10.90	10.99	1.90±0.30
92	2MASSJ005055.7+293328	-0.33±0.04	10.0	-0.12±0.02	19.6	<0.036	10.95	10.98	10.97	11.03	1.20±0.30
93	2MASSJ010230.1+262337	-0.18±0.21	9.9	-0.15±0.17	16.4	<0.153	10.97	10.81	10.79	10.77	0.46±0.50
94	2MASSJ010835.1+214818	-0.17±0.03	9.6	0.07±0.01	19.0	0.039±0.007	11.70	11.79	11.80	11.78	1.71±0.30
95	2MASSJ012031.5+200327	-0.89±1.07	10.0	-0.69±0.50	16.1	0.693±0.188	9.87	9.43	9.57	9.75	0.37±0.50
96	2MASSJ015721.0+171248	-0.74±0.18	10.2	-0.36±0.08	16.5	0.083±0.021	11.24	11.08	11.10	11.25	1.77±0.30
97	2MASSJ022150.6+132741	0.04±0.02	11.9	0.07±0.02	15.5	<0.071	11.09	11.20	11.22	11.34	1.61±0.30
98	2MASSJ024807.3+145957	0.04±0.11	11.2	-0.08±0.10	18.6	<0.109	10.48	10.55	10.52	10.53	0.49±0.50
99	2MASSJ034857.6+125547	-0.50±0.03	10.1	-0.27±0.01	16.8	<0.013	12.00	11.84	11.79	11.85	1.84±0.30
100	2MASSJ081652.2+425829	0.39±0.12	10.4	0.16±0.08	19.6	<0.139	11.01	10.83	10.82	10.64	<0.94
101	2MASSJ082311.3+435318	0.14±0.09	11.8	0.19±0.07	16.2	<0.135	11.20	11.35	11.36	11.34	1.67±0.30
102	2MASSJ091848.6+211717	-0.13±0.03	11.2	0.06±0.04	15.7	0.099±0.013	11.17	11.21	11.22	11.28	1.38±0.30
103	2MASSJ092049.0+190320	-0.70±0.41	9.9	-0.38±0.16	16.2	<0.199	10.16	10.31	10.37	10.51	<0.65
104	2MASSJ094636.4+205610	0.20±0.16	10.4	0.19±0.12	19.6	<0.201	11.63	11.52	11.56	11.45	1.37±0.30
105	2MASSJ095504.5+170556	0.18±0.09	10.2	0.28±0.05	19.5	<0.100	10.75	10.60	10.59	10.41	0.09±0.50
106	2MASSJ100121.1+215011	-0.95±0.94	10.3	-0.50±0.16	16.7	0.434±0.062	11.24	11.03	10.99	11.29	1.88±0.30
107	2MASSJ101400.4+194614										1.08±0.30



TABLE 4 — *Continued*

ID	Name	Str <sub>9.7μm-Sil</sub>	$\lambda_{9.7\mu\text{m-Sil}}^{\text{peak}}$ [μm]	Str <sub>18μm-Sil</sub>	$\lambda_{18\mu\text{m-Sil}}^{\text{peak}}$ [μm]	EW <sub>11.3μmPAH</sub> [μm]	Log $L_{5\mu\text{m}}$ [log( $L_{\odot}$ )]	Log $L_{15\mu\text{m}}$ [log( $L_{\odot}$ )]	Log $L_{18\mu\text{m}}$ [log( $L_{\odot}$ )]
108	2MASSiJ101649.3+215435	0.19±0.11	10.4	0.14±0.07	20.5	<0.128	11.15	11.11	11.19
109	2MASSiJ102724.9+121920	-0.24±0.07	9.8	-0.05±0.03	16.4	0.043±0.014	11.61	11.61	11.63
110	2MASSiJ105144.2+353930	-0.36±0.07	10.0	0.12±0.03	16.9	<0.062	10.73	10.88	10.90
111	2MASSiJ125807.4+232921	-0.35±0.03	10.1	-0.13±0.01	16.5	<0.019	11.61	11.69	11.67
112	2MASSiJ130005.3+163214	-0.21±0.03	9.9	-0.05±0.02	15.2	<0.030	11.02	11.01	10.99
113	2MASSiJ130700.6+233805	-1.59±0.06	10.4	-0.54±0.01	17.1	0.032±0.005	11.95	11.77	11.70
114	2MASSiJ132917.5+121340	0.11±0.16	11.1	-0.12±0.19	16.4	<0.199	10.78	10.76	10.72
115	2MASSiJ134915.2+220032								
116	2MASSiJ140251.1+263117	0.10±0.04	11.8	0.12±0.04	19.0	<0.068	11.20	11.01	10.99
117	2MASSiJ145331.5+135358	-1.78±0.07	10.1	-0.37±0.01	17.9	0.041±0.005	11.25	11.21	11.19
118	2MASSiJ145406.6+195028	-0.43±0.19	10.5	-0.37±0.13	16.7	0.169±0.052	11.14	10.98	11.01
119	2MASSiJ145410.1+195648	-0.26±0.25	9.9	-0.12±0.13	16.4	<0.132	11.47	11.28	11.27
120	2MASSiJ145608.6+275008	0.14±0.09	10.9	0.07±0.07	19.0	<0.160	11.41	11.26	11.28
121	2MASSiJ150113.1+232908	0.14±0.03	11.9	0.07±0.01	18.4	<0.042	11.41	11.45	11.53
122	2MASSiJ151621.1+225944	-0.09±0.14	11.2	-0.39±0.22	16.5	0.208±0.068	11.06	10.81	10.81
123	2MASSiJ151653.2+190048	0.25±0.02	10.1	0.10±0.01	19.0	<0.032	11.89	11.68	11.67
124	2MASSiJ151901.5+183804	0.37±0.07	11.7	-0.11±0.09	15.7	<0.213	10.75	10.46	10.51
125	2MASSiJ152151.0+225120	-0.25±0.20	10.0	-0.28±0.11	16.5	<0.137	11.45	11.59	11.62
126	2MASSiJ154307.7+193751	-0.12±0.08	12.1	0.08±0.05	20.4	0.094±0.024	11.71	11.64	11.64
127	2MASSiJ163700.2+222114	-0.11±0.07	9.8	0.08±0.03	18.7	0.205±0.021	10.67	10.68	10.64
128	2MASSiJ163736.5+254302	-0.39±0.21	10.0	-0.51±0.20	16.5	<0.182	11.38	11.44	11.49
129	2MASSiJ165939.7+183436	-0.23±0.02	10.6	-0.16±0.01	16.4	0.027±0.004	11.32	11.53	11.54
130	2MASSiJ170536.6+210137	0.10±0.12	12.4	-0.38±0.18	15.5	0.486±0.063	10.77	10.73	10.92
131	2MASSiJ171442.7+260248	0.02±0.03	11.6	-0.30±0.04	19.6	<0.053	11.09	10.98	10.88
132	2MASSiJ222221.1+195947	0.19±0.02	11.2	0.15±0.02	19.0	<0.038	11.40	11.35	11.35
133	2MASSiJ222554.2+195837	-0.61±0.05	10.0	-0.08±0.02	18.7	<0.037	10.86	10.94	10.90
134	2MASSiJ223742.6+145614	0.19±0.10	10.7	-0.21±0.11	16.3	0.229±0.049	11.22	11.13	11.20
135	2MASSiJ223946.0+192955	0.37±0.14	12.3	-0.44±0.30	16.3	1.134±0.287	10.57	10.31	10.42
136	2MASSiJ230304.3+162440	-0.90±0.60	10.0	-1.16±0.29	17.5	1.186±0.082	10.20	10.26	10.69
137	2MASSiJ230442.4+270616	0.29±0.19	10.6	0.29±0.08	19.6	<0.338	10.37	10.35	10.47
138	2MASSiJ234259.3+134750	0.29±0.15	10.1	-0.25±0.12	15.1	<0.161	11.10	11.11	11.25
139	2MASSiJ234449.5+122143	0.10±0.04	11.2	0.04±0.02	20.5	<0.054	11.26	11.29	11.32

TABLE 5  
THE MEDIAN COMPOSITE SPECTRA OF PG AND 2MASS SAMPLES

wave[ $\mu\text{m}$ ]	$\log(\nu L_\nu)$ All PG	$\log(\nu L_\nu)$ Radio-quiete PG	$\log(\nu L_\nu)$ Radio-loud PG	$\log(\nu L_\nu)$ All 2MASS
5.05	0.035 $\pm$ 0.151	0.049 $\pm$ 0.165	0.013 $\pm$ 0.096	0.024 $\pm$ 0.206
5.15	0.021 $\pm$ 0.156	0.032 $\pm$ 0.171	-0.006 $\pm$ 0.097	0.014 $\pm$ 0.191
5.25	0.023 $\pm$ 0.161	0.024 $\pm$ 0.174	0.023 $\pm$ 0.096	0.008 $\pm$ 0.246
5.36	-0.002 $\pm$ 0.173	-0.002 $\pm$ 0.186	0.001 $\pm$ 0.102	0.006 $\pm$ 0.209
5.47	0.001 $\pm$ 0.159	-0.000 $\pm$ 0.169	0.004 $\pm$ 0.101	0.020 $\pm$ 0.229
5.58	-0.003 $\pm$ 0.164	-0.006 $\pm$ 0.176	-0.001 $\pm$ 0.099	0.029 $\pm$ 0.191
5.69	-0.005 $\pm$ 0.150	-0.019 $\pm$ 0.160	0.009 $\pm$ 0.098	0.025 $\pm$ 0.150
5.80	-0.010 $\pm$ 0.175	-0.017 $\pm$ 0.189	0.011 $\pm$ 0.088	-0.001 $\pm$ 0.201
5.92	-0.009 $\pm$ 0.154	-0.009 $\pm$ 0.166	0.002 $\pm$ 0.089	0.006 $\pm$ 0.170
6.04	-0.014 $\pm$ 0.146	-0.017 $\pm$ 0.156	0.013 $\pm$ 0.085	0.018 $\pm$ 0.192
6.16	-0.006 $\pm$ 0.145	-0.006 $\pm$ 0.156	-0.001 $\pm$ 0.083	0.038 $\pm$ 0.158
6.28	-0.007 $\pm$ 0.136	-0.008 $\pm$ 0.147	-0.005 $\pm$ 0.080	0.050 $\pm$ 0.167
6.40	-0.010 $\pm$ 0.135	-0.013 $\pm$ 0.145	-0.004 $\pm$ 0.084	0.022 $\pm$ 0.142
6.53	-0.026 $\pm$ 0.137	-0.031 $\pm$ 0.148	-0.003 $\pm$ 0.080	-0.007 $\pm$ 0.146
6.66	-0.027 $\pm$ 0.137	-0.034 $\pm$ 0.147	-0.015 $\pm$ 0.078	-0.013 $\pm$ 0.155
6.80	-0.025 $\pm$ 0.125	-0.028 $\pm$ 0.135	-0.016 $\pm$ 0.075	-0.008 $\pm$ 0.141
6.93	-0.022 $\pm$ 0.123	-0.029 $\pm$ 0.133	-0.013 $\pm$ 0.074	0.020 $\pm$ 0.179
7.07	-0.028 $\pm$ 0.121	-0.034 $\pm$ 0.130	-0.021 $\pm$ 0.074	0.012 $\pm$ 0.152
7.21	-0.032 $\pm$ 0.119	-0.035 $\pm$ 0.128	-0.022 $\pm$ 0.072	0.019 $\pm$ 0.139
7.36	-0.032 $\pm$ 0.131	-0.033 $\pm$ 0.144	-0.031 $\pm$ 0.068	0.033 $\pm$ 0.150
7.50	-0.025 $\pm$ 0.132	-0.029 $\pm$ 0.145	-0.023 $\pm$ 0.071	0.051 $\pm$ 0.184
7.65	-0.017 $\pm$ 0.119	-0.017 $\pm$ 0.128	-0.017 $\pm$ 0.076	0.072 $\pm$ 0.198
7.81	-0.031 $\pm$ 0.113	-0.015 $\pm$ 0.122	-0.031 $\pm$ 0.069	0.051 $\pm$ 0.199
7.96	-0.033 $\pm$ 0.106	-0.023 $\pm$ 0.113	-0.034 $\pm$ 0.069	0.034 $\pm$ 0.176
8.12	-0.042 $\pm$ 0.105	-0.025 $\pm$ 0.113	-0.045 $\pm$ 0.062	0.041 $\pm$ 0.145
8.29	-0.049 $\pm$ 0.149	-0.049 $\pm$ 0.165	-0.049 $\pm$ 0.057	0.017 $\pm$ 0.154
8.45	-0.049 $\pm$ 0.104	-0.048 $\pm$ 0.113	-0.053 $\pm$ 0.053	0.019 $\pm$ 0.149
8.62	-0.042 $\pm$ 0.111	-0.046 $\pm$ 0.121	-0.040 $\pm$ 0.054	0.025 $\pm$ 0.150
8.79	-0.034 $\pm$ 0.114	-0.036 $\pm$ 0.124	-0.033 $\pm$ 0.060	-0.010 $\pm$ 0.121
8.97	-0.035 $\pm$ 0.100	-0.045 $\pm$ 0.109	-0.023 $\pm$ 0.049	-0.027 $\pm$ 0.128
9.15	-0.020 $\pm$ 0.106	-0.036 $\pm$ 0.116	-0.003 $\pm$ 0.051	-0.042 $\pm$ 0.155
9.33	-0.014 $\pm$ 0.105	-0.025 $\pm$ 0.114	0.006 $\pm$ 0.052	-0.066 $\pm$ 0.174
9.52	0.011 $\pm$ 0.103	-0.009 $\pm$ 0.111	0.028 $\pm$ 0.053	-0.066 $\pm$ 0.176
9.71	0.017 $\pm$ 0.106	-0.002 $\pm$ 0.113	0.049 $\pm$ 0.054	-0.051 $\pm$ 0.200
9.90	0.024 $\pm$ 0.099	0.009 $\pm$ 0.106	0.042 $\pm$ 0.054	-0.081 $\pm$ 0.222
10.10	0.023 $\pm$ 0.096	0.019 $\pm$ 0.103	0.062 $\pm$ 0.051	-0.035 $\pm$ 0.170
10.30	0.026 $\pm$ 0.115	0.020 $\pm$ 0.123	0.068 $\pm$ 0.058	-0.026 $\pm$ 0.154
10.51	0.047 $\pm$ 0.087	0.033 $\pm$ 0.091	0.088 $\pm$ 0.050	0.003 $\pm$ 0.188
10.72	0.030 $\pm$ 0.091	0.020 $\pm$ 0.096	0.082 $\pm$ 0.053	-0.012 $\pm$ 0.161
10.93	0.038 $\pm$ 0.095	0.025 $\pm$ 0.100	0.066 $\pm$ 0.051	0.018 $\pm$ 0.142
11.15	0.047 $\pm$ 0.084	0.041 $\pm$ 0.090	0.069 $\pm$ 0.048	0.047 $\pm$ 0.155
11.37	0.048 $\pm$ 0.097	0.048 $\pm$ 0.105	0.055 $\pm$ 0.049	0.046 $\pm$ 0.167
11.60	0.031 $\pm$ 0.072	0.022 $\pm$ 0.076	0.055 $\pm$ 0.046	0.032 $\pm$ 0.115
11.83	0.021 $\pm$ 0.076	0.019 $\pm$ 0.082	0.044 $\pm$ 0.038	0.025 $\pm$ 0.099
12.07	0.023 $\pm$ 0.063	0.018 $\pm$ 0.067	0.032 $\pm$ 0.038	0.030 $\pm$ 0.098
12.31	0.006 $\pm$ 0.050	0.007 $\pm$ 0.054	0.005 $\pm$ 0.034	0.030 $\pm$ 0.107
12.56	0.002 $\pm$ 0.047	0.001 $\pm$ 0.051	0.002 $\pm$ 0.029	0.044 $\pm$ 0.113
12.81	0.005 $\pm$ 0.046	0.006 $\pm$ 0.049	0.001 $\pm$ 0.030	0.050 $\pm$ 0.148
13.06	-0.011 $\pm$ 0.041	-0.009 $\pm$ 0.044	-0.016 $\pm$ 0.026	0.024 $\pm$ 0.071
13.33	-0.017 $\pm$ 0.035	-0.012 $\pm$ 0.037	-0.022 $\pm$ 0.022	0.002 $\pm$ 0.064
13.59	-0.017 $\pm$ 0.030	-0.015 $\pm$ 0.032	-0.020 $\pm$ 0.020	0.005 $\pm$ 0.066
13.86	-0.020 $\pm$ 0.025	-0.016 $\pm$ 0.026	-0.026 $\pm$ 0.017	-0.004 $\pm$ 0.050
14.14	-0.014 $\pm$ 0.021	-0.013 $\pm$ 0.020	-0.015 $\pm$ 0.022	0.005 $\pm$ 0.044
14.42	-0.007 $\pm$ 0.020	-0.007 $\pm$ 0.020	-0.009 $\pm$ 0.019	0.014 $\pm$ 0.059
14.71	-0.012 $\pm$ 0.018	-0.012 $\pm$ 0.017	-0.010 $\pm$ 0.020	-0.002 $\pm$ 0.047
15.01	-0.010 $\pm$ 0.016	-0.010 $\pm$ 0.016	-0.007 $\pm$ 0.017	-0.015 $\pm$ 0.047
15.31	-0.002 $\pm$ 0.020	-0.001 $\pm$ 0.016	-0.004 $\pm$ 0.033	-0.013 $\pm$ 0.059
15.61	0.024 $\pm$ 0.027	0.024 $\pm$ 0.026	0.028 $\pm$ 0.029	0.014 $\pm$ 0.067
15.93	0.015 $\pm$ 0.022	0.015 $\pm$ 0.021	0.015 $\pm$ 0.025	-0.011 $\pm$ 0.071
16.24	0.018 $\pm$ 0.023	0.018 $\pm$ 0.023	0.021 $\pm$ 0.023	-0.005 $\pm$ 0.069
16.57	0.024 $\pm$ 0.027	0.025 $\pm$ 0.028	0.021 $\pm$ 0.025	0.004 $\pm$ 0.091
16.90	0.028 $\pm$ 0.031	0.028 $\pm$ 0.031	0.027 $\pm$ 0.030	0.006 $\pm$ 0.097
17.24	0.024 $\pm$ 0.036	0.025 $\pm$ 0.037	0.024 $\pm$ 0.031	0.009 $\pm$ 0.106
17.58	0.025 $\pm$ 0.038	0.027 $\pm$ 0.038	0.019 $\pm$ 0.039	0.000 $\pm$ 0.107
17.94	0.019 $\pm$ 0.036	0.019 $\pm$ 0.035	0.019 $\pm$ 0.037	-0.005 $\pm$ 0.158
18.29	0.015 $\pm$ 0.038	0.014 $\pm$ 0.038	0.021 $\pm$ 0.038	-0.003 $\pm$ 0.071
18.66	0.018 $\pm$ 0.043	0.021 $\pm$ 0.045	0.013 $\pm$ 0.036	0.018 $\pm$ 0.100
19.03	0.007 $\pm$ 0.043	0.006 $\pm$ 0.044	0.010 $\pm$ 0.036	-0.003 $\pm$ 0.116
19.41	-0.003 $\pm$ 0.044	-0.003 $\pm$ 0.045	-0.007 $\pm$ 0.038	0.006 $\pm$ 0.084
19.80	-0.006 $\pm$ 0.046	-0.009 $\pm$ 0.047	-0.001 $\pm$ 0.043	0.012 $\pm$ 0.098
20.20	-0.016 $\pm$ 0.053	-0.021 $\pm$ 0.053	-0.007 $\pm$ 0.051	0.011 $\pm$ 0.098
20.60	-0.027 $\pm$ 0.055	-0.031 $\pm$ 0.056	-0.013 $\pm$ 0.052	0.013 $\pm$ 0.117
21.01	-0.021 $\pm$ 0.061	-0.028 $\pm$ 0.064	-0.014 $\pm$ 0.049	0.014 $\pm$ 0.098
21.43	-0.028 $\pm$ 0.068	-0.032 $\pm$ 0.069	-0.026 $\pm$ 0.063	0.014 $\pm$ 0.111
21.86	-0.032 $\pm$ 0.070	-0.036 $\pm$ 0.072	-0.029 $\pm$ 0.061	0.016 $\pm$ 0.121

TABLE 5 — *Continued*

wave[ $\mu\text{m}$ ]	$\log(\nu L_\nu)$ All PG	$\log(\nu L_\nu)$ Radio-quiete PG	$\log(\nu L_\nu)$ Radio-loud PG	$\log(\nu L_\nu)$ All 2MASS
22.30	-0.037 $\pm$ 0.074	-0.036 $\pm$ 0.076	-0.045 $\pm$ 0.067	0.010 $\pm$ 0.114
22.75	-0.046 $\pm$ 0.078	-0.045 $\pm$ 0.081	-0.048 $\pm$ 0.060	0.015 $\pm$ 0.122
23.20	-0.051 $\pm$ 0.083	-0.050 $\pm$ 0.086	-0.051 $\pm$ 0.069	0.013 $\pm$ 0.134
23.66	-0.056 $\pm$ 0.098	-0.054 $\pm$ 0.103	-0.066 $\pm$ 0.071	0.011 $\pm$ 0.143
24.14	-0.059 $\pm$ 0.093	-0.058 $\pm$ 0.097	-0.064 $\pm$ 0.074	0.017 $\pm$ 0.144
24.62	-0.066 $\pm$ 0.102	-0.066 $\pm$ 0.106	-0.067 $\pm$ 0.081	0.005 $\pm$ 0.154
25.11	-0.079 $\pm$ 0.105	-0.080 $\pm$ 0.110	-0.065 $\pm$ 0.078	0.001 $\pm$ 0.156
55.00	-0.301 $\pm$ 0.270	-0.303 $\pm$ 0.276	-0.301 $\pm$ 0.249	-0.090 $\pm$ 0.442
130.00	-0.611 $\pm$ 0.295	-0.611 $\pm$ 0.290	-0.601 $\pm$ 0.317	-0.251 $\pm$ 0.442

NOTE. —

TABLE 6  
CORRELATION BETWEEN DIFFERENT IR COLOR AND 15  $\mu\text{m}$  LUMINOSITY

Y vs. X	A	B	$\sigma$
$\log(L_{25\mu\text{m}}/L_{15\mu\text{m}})$ vs. $\log(L_{15\mu\text{m}})$	-0.19	0.014	0.14
$\log(L_{25\mu\text{m}}/L_{5\mu\text{m}})$ vs. $\log(L_{15\mu\text{m}})$	-0.37	0.028	0.23
$\log(L_{15\mu\text{m}}/L_{5\mu\text{m}})$ vs. $\log(L_{15\mu\text{m}})$	-0.18	0.014	0.16

NOTE. —  $Y = (A + BX) \pm \sigma$ . The monochromatic luminosity is defined to be the average emission over a 2  $\mu\text{m}$  width.